exoALMA. XII. Weighing and sizing exoALMA disks with rotation curve modelling

Longarini, C.; Lodato, G.; Rosotti, G.; Andrews, S.; Winter, A.; Stadler, J.; ... ; Zawadzki, B.

Note: To cite this publication please use the final published version (if applicable).

exoALMA. XII. Weighing and Sizing exoALMA Disks with Rotation Curve Modelling

Cristiano Longarini[1,2], Giuseppe Lodato[2], Giovanni Rosotti[2], Sean Andrews[3], Andrew Winter[4,5], Jochen Stadler[4,6], Andrés Izquierdo[7,8,9], Maria Galloway-Sprietsma[9], Stefano Facchini[2], Pietro Curone[2,10], Myriam Benisty[4,5], Richard Teague[11], Jaehan Bae[9], Marcelo Barraza-Alfaro[11], Gianni Cataldi[12], Ian Czekala[13], Nicolás Cuello[6], Daniele Fasano[4,5], Mario Flock[5], Misato Fukagawa[12], Himanshi Garg[14], Cassandra Hall[15,16,17], Iain Hammond[14], Caitlyn Hardiman[14], Thomas Hilder[14], Jane Huang[18], John D. Ilee[19], Andrea Isella[20,21], Kazuhiro Kanagawa[22], Geoffroy Lesur[6], Ryan A. Loomis[23], Francois Ménard[6], Ryuta Orihara[22], Christophe Pinte[6,14], Daniel Price[14], Leonardo Testi[24], Gaylor Wafflard-Fernandez[6], Lisa Wölfer[11], Hsi-Wei Yen[25], Tomohiro C. Yoshida[12,26], and Brianna Zawadzki[27]

[1] Institute of Astronomy, University of Cambridge, Madingley Road, Cambridge, CB3 0HA, UK; cl2000@cam.ac.uk
[2] Dipartimento di Fisica, Università degli Studi di Milano, Via Celoria 16, Milano, 20133, Italy
[3] Center for Astrophysics—Harvard & Smithsonian, Cambridge, MA 02138, USA
[4] Université Côte d'Azur, Observatoire de la Côte d'Azur, CNRS, Laboratoire Lagrange, 06300 Nice, France
[5] Max-Planck Institute for Astronomy (MPIA), Königstuhl 17, 69117 Heidelberg, Germany
[6] Université Grenoble Alpes, CNRS, IPAG, 38000 Grenoble, France
[7] Leiden Observatory, Leiden University, P.O. Box 9513, NL-2300 RA Leiden, The Netherlands
[8] European Southern Observatory, Karl-Schwarzschild-Str. 2, D-85748 Garching bei München, Germany
[9] Department of Astronomy, University of Florida, Gainesville, FL 32611, USA
[10] Departamento de Astronomía, Universidad de Chile, Camino El Observatorio 1515, Las Condes, Santiago, Chile
[11] Department of Earth, Atmospheric, and Planetary Sciences, Massachusetts Institute of Technology, Cambridge, MA 02139, USA
[12] National Astronomical Observatory of Japan, Osawa 2-21-1, Mitaka, Tokyo 181-8588, Japan
[13] School of Physics & Astronomy, University of St. Andrews, North Haugh, St. Andrews KY16 9SS, UK
[14] School of Physics and Astronomy, Monash University, VIC 3800, Australia
[15] Department of Physics and Astronomy, The University of Georgia, Athens, GA 30602, USA
[16] Center for Simulational Physics, The University of Georgia, Athens, GA 30602, USA
[17] Institute for Artificial Intelligence, The University of Georgia, Athens, GA 30602, USA
[18] Department of Astronomy, Columbia University, 538 W. 120th Street, Pupin Hall, New York, NY 10027, USA
[19] School of Physics and Astronomy, University of Leeds, Leeds, LS2 9JT, UK
[20] Department of Physics and Astronomy, Rice University, 6100 Main Street, Houston, TX 77005, USA
[21] Rice Space Institute, Rice University, 6100 Main Street, Houston, TX 77005, USA
[22] College of Science, Ibaraki University, 2-1-1 Bunkyo, Mito, Ibaraki 310-8512, Japan
[23] National Radio Astronomy Observatory, 520 Edgemont Road, Charlottesville, VA 22903, USA
[24] Dipartimento di Fisica e Astronomia, Universita' di Bologna, I-40190 Bologna, Italy
[25] Academia Sinica Institute of Astronomy & Astrophysics, 11F of Astronomy-Mathematics Building, AS/NTU, No.1, Sec. 4, Roosevelt Road, Taipei 106216, Taiwan
[26] Department of Astronomical Science, The Graduate University for Advanced Studies, SOKENDAI, 2-21-1 Osawa, Mitaka, Tokyo 181-8588, Japan
[27] Department of Astronomy, Van Vleck Observatory, Wesleyan University, 96 Foss Hill Drive, Middletown, CT 06459, USA

Received 2024 November 25; revised 2025 February 17; accepted 2025 February 28; published 2025 April 28

Abstract

The exoALMA large program offers a unique opportunity to investigate the fundamental properties of protoplanetary disks, such as their masses and sizes, providing important insights into the mechanism responsible for the transport of angular momentum. In this work, we model the rotation curves of CO isotopologues ^{12}CO and ^{13}CO of 10 sources within the exoALMA sample, and we constrain the stellar mass, the disk mass, and the density scale radius through precise characterization of the pressure gradient and disk self-gravity. We obtain dynamical disk masses for our sample by measuring the self-gravitating contribution to the gravitational potential. We are able to parametrically describe their surface density, and all of them appear gravitationally stable. By combining dynamical disk masses with dust continuum emission data, we determine an averaged gas-to-dust ratio of approximately 400, not statistically consistent with the standard value of 100, assuming optically thin dust emission. In addition, the measurement of the dynamical scale radius allows for direct comparison with flux-based radii of gas and dust. This comparison suggests that substructures may influence the size of the dust disk and that CO depletion might reconcile our measurements with thermochemical models. Finally, with the stellar mass, disk mass, scale radius, and accretion rate, and assuming self-similar evolution of the surface density, we constrain the effective α_S for these systems. We find a broad range of α_S values ranging between 10^{-5} and 10^{-2}.

Unified Astronomy Thesaurus concepts: Protoplanetary disks (1300); Planet formation (1241); Stellar accretion disks (1579)

1. Introduction

A particularly important quantity in protoplanetary disk kinematics is the rotation curve, i.e., the azimuthally averaged rotational velocity as a function of the radius. Indeed, in a protoplanetary disk, the dominant motion is azimuthal

(C. Pinte et al. 2023); hence having a thorough model of the rotation curve is crucial to precisely characterize such environments. On top of the standard Keplerian rotation, there are additional effects that globally influence the rotation curve, such as the pressure gradient and the disk self-gravity, whose strengths are connected to fundamental disk quantities. Recently, significant work has been done to characterize rotation curves in protoplanetary disks. Leveraging the analytical work by G. Bertin & G. Lodato (1999) and B. Veronesi et al. (2021) constrained the star and disk masses of the protoplanetary disk Elias 2–27 from the rotation curves of ^{13}CO and C^{18}O, marking the first dynamical estimate of a protoplanetary disk mass. Subsequent developments have introduced new methods for extracting rotation curves (e.g., A. F. Izquierdo et al. 2021, 2023), enhancing the quality of modeling. G. Lodato et al. (2023) presented a model for the rotation curve of a vertically isothermal disk including self-gravity, applying it to IM Lup and GM Aur. Following this, P. Martire et al. (2024) generalized the model for a vertically stratified disk and applied it to the MAPS sample. Most recently, B. Veronesi et al. (2024) and S. M. Andrews et al. (2024) studied the uncertainties related to this method, finding that the precision of disk mass measurements is around 25%, with the minimum measurable mass being 5% the stellar mass, and that it is possible to constrain surface density profile, rather than just the integrated mass.

In this work, we model the rotation curves of the sample described in J. Stadler et al. (2025), extracted with DISCMINER (A. Izquierdo et al. 2025), to constrain stellar masses, disk masses, and scale radii, following the approach of the aforementioned Letters. This Letter is organized as follows. In Section 2, we briefly present the physical model we adopt to describe the rotation curve. We use a thermally stratified model (P. Martire et al. 2024), where the thermal structure is obtained in M. Galloway-Sprietsma et al. (2025). In Section 3, we present the analysis procedure, justify the sample we are analyzing, and discuss how we treat the systematic uncertainties. In Section 4, we present the results and separately discuss the disk masses, stellar masses, scale radii, and properties we can extract from them. Finally, in Section 5, we summarize the findings and draw conclusions.

2. Physical Model

The model we adopt to describe the rotation curve of a protoplanetary disk is the one presented in G. Lodato et al. (2023), then generalized by P. Martire et al. (2024) including the disk thermal stratification. The need for including thermal stratification is justified in J. Stadler et al. (2025), showing that the shift between ^{12}CO and ^{13}CO rotation curves cannot be explained by a vertical isothermal model. The full description of the stratified model is given in Appendix A.

2.1. 2D Temperature Structure

There is observational evidence that protoplanetary disks have a vertical temperature gradient (E. Dartois et al. 2003; K. A. Rosenfeld et al. 2013; C. Pinte et al. 2018). The thermal structure can be probed through optically thick molecular line emission (C. J. Law et al. 2021). M. Galloway-Sprietsma et al. (2025) obtained the 2D thermal structures of exoALMA disks from ^{12}CO and ^{13}CO data cubes, adopting the Dartois

(E. Dartois et al. 2003) prescription

$$T(R, z) = \begin{cases} T_{\text{atm}} + (T_{\text{mid}} - T_{\text{atm}}) \cos^2\left(\dfrac{\pi z}{2 Z_q}\right), & z < Z_q, \\ \\ T_{\text{atm}}, & z > Z_q \end{cases}$$
(1)

where

$$\begin{aligned} T_{\text{atm}}(R) &= T_{\text{atm},100}(R/100\,\text{au})^{q_{\text{atm}}} \\ T_{\text{mid}}(R) &= T_{\text{mid},100}(R/100\,\text{au})^{q_{\text{mid}}} \\ Z_q &= Z_0(R/100\,\text{au})^{\beta}. \end{aligned}$$
(2)

Hence, the 2D thermal structure is described by six parameters, namely, $T_{\text{mid},100}$, $T_{\text{atm},100}$, q_{mid}, q_{atm}, Z_0, and β. In this work, we will use the Dartois prescription with the best-fit values for the thermal parameters obtained by M. Galloway-Sprietsma et al. (2025), which are summarized in Appendix C.

2.2. Model for the Rotation Curve

In this paragraph, we present the fundamental equations of the stratified model from P. Martire et al. (2024). The complete derivation of the rotation curve is given in Appendix A.

Under the hypothesis of self-similar surface density profile (D. Lynden-Bell & J. E. Pringle 1974)

$$\Sigma(R) = \frac{(2 - \gamma)M_d}{2\pi R_c^2}\left(\frac{R}{R_c}\right)^{-\gamma} \exp\left[-\left(\frac{R}{R_c}\right)^{2-\gamma}\right],$$
(3)

and assuming a temperature structure

$$T(R, z) = T_{\text{mid}}(R)f(R, z),$$
(4)

with f given by Equation (1). P. Martire et al. (2024) showed that the rotation curve is given by

$$v_\phi^2 = v_k^2 \left\{\left[1 + \left(\frac{z}{R}\right)^2\right]^{-3/2} - \left[\gamma' + (2 - \gamma)\left(\frac{R}{R_c}\right)^{2-\gamma} - \right.\right.$$
$$\left.\left. - \frac{\mathrm{d}\log(fg)}{\mathrm{d}\log R}\right]\left(\frac{H}{R}\right)_{\text{mid}}^2 f(R, z)\right\} + v_d^2,$$
(5)

where $\gamma' = \gamma + (3 + q_{\text{mid}})/2$, $v_k = \sqrt{GM_\star/R}$,

$$\log(fg) = -\frac{1}{H_{\text{mid}}^2}\int_0^z \frac{z'}{f}\left[1 + \left(\frac{z'}{R}\right)^2\right]^{-3/2} \mathrm{d}z'.$$
(6)

and

$$v_d^2 = G\int_0^\infty \left[K(k) - \frac{1}{4}\left(\frac{k^2}{1 - k^2}\right)\times\right.$$
$$\left.\times\left(\frac{R'}{R} - \frac{R}{r} + \frac{z^2}{RR'}\right)E(k)\right]\sqrt{\frac{R'}{R}}k\Sigma(R')dR',$$
(7)

where $K(k)$ and $E(k)$ are complete elliptic integrals (M. Abramowitz & I. A. Stegun 1970) and $k^2 = 4RR'/[(R + R')^2 + z^2]$.

The model presented in this section does not account for pressure-modulated substructures that may be present in the data. To assess their influence on the best-fit parameters, we tested a rotation curve model that includes the contribution of substructures in the pressure gradient. In particular, we modeled the density variations associated with gaps and rings as Gaussians and then computed the pressure gradient and disk self-gravity self-consistently. The corresponding velocity

Table 1
Summary of the Main Results of This Work

Source	$M_\star$ $(M_\odot)$	M_d $(M_\odot)$	R_c (au)	$M_d/M_\star$	σ_{M_d}/M_d	$M_{\mathrm{discminer}}$	$\Delta M_\star/M_\star$ (%)	M_{dust} (M_J)	g/d
AA Tau	$0.624^{+0.033}_{-0.035}$	$0.155^{+0.036}_{-0.036}$	156^{+106}_{-41}	$0.25^{+0.06}_{-0.06}$	0.23	0.791	26.7%	0.115	1417^{+326}_{-330}
DM Tau	$0.468^{+0.014}_{-0.015}$	$0.057^{+0.019}_{-0.020}$	240^{+42}_{-27}	$0.12^{+0.04}_{-0.04}$	0.34	0.453	-3.1%	0.162	367^{+131}_{-121}
HD 34282	$1.520^{+0.025}_{-0.031}$	$0.143^{+0.045}_{-0.041}$	370^{+109}_{-78}	$0.09^{+0.03}_{-0.03}$	0.30	1.620	6.6%	1.091	137^{+40}_{-43}
J1615	$1.105^{+0.011}_{-0.012}$	$0.082^{+0.014}_{-0.014}$	167^{+20}_{-15}	$0.07^{+0.01}_{-0.01}$	0.18	1.140	3.1%	0.308	279^{+49}_{-49}
J1842	$1.042^{+0.010}_{-0.011}$	$0.078^{+0.013}_{-0.014}$	231^{+12}_{-50}	$0.07^{+0.01}_{-0.01}$	0.18	1.068	2.5%	0.108	759^{+134}_{-129}
J1852[a]	$1.022^{+0.021}_{-0.021}$	$0.044^{+0.024}_{-0.032}$	87^{+69}_{-16}	$0.04^{+0.02}_{-0.03}$	0.65	1.028	0.6%	0.110	420^{+300}_{-301}
LkCa 15	$1.118^{+0.013}_{-0.015}$	$0.108^{+0.016}_{-0.016}$	150^{+12}_{-16}	$0.10^{+0.01}_{-0.01}$	0.15	1.028	-8.0%	0.333	339^{+49}_{-50}
PDS 66[a]	$1.299^{+0.036}_{-0.101}$	$0.038^{+0.099}_{-0.035}$	28^{+12}_{-5}	$0.03^{+0.08}_{-0.03}$	1.76	1.277	-1.7%	0.108	364^{+342}_{-357}
SY Cha	$0.812^{+0.037}_{-0.041}$	$0.084^{+0.044}_{-0.043}$	112^{+21}_{-15}	$0.10^{+0.05}_{-0.05}$	0.52	0.813	0.1%	0.170	517^{+266}_{-273}
V4046 Sgr[a]	$1.777^{+0.005}_{-0.006}$	$0.058^{+0.006}_{-0.006}$	99^{+5}_{-5}	$0.03^{+0.00}_{-0.00}$	0.11	1.763	-0.8%	0.112	540^{+60}_{-59}

Notes. Best-fit values for the stellar mass, disk mass, and scale radius with the relative uncertainties from the posterior distributions, disk-to-star mass ratio with propagated errors, disk mass relative uncertainty, stellar mass from DISCMINER fit (A. Izquierdo et al. 2025), percentage difference from the dynamical stellar mass estimate and the DISCMINER one, dust mass from continuum emission from P. Curone et al. (2025), and gas-to-dust ratio. The value σ_{M_d}/M_d represents the average of asymmetric uncertainties (upper and lower) on the disk mass. The errors on the disk-to-star mass ratio and on the gas-to-dust ratio have been computed using the posterior distributions for the relevant quantities.
[a] These sources have a disk-to-star mass ratio <0.05, the theoretical limit for disk mass detection (S. M. Andrews et al. 2024; B. Veronesi et al. 2024). We report the best-fit values obtained through the fitting procedure, regardless of the disk mass limit. In the figures, these sources are labeled with a diamond rather than a square.

perturbations are on the order of 50–70 m s^{-1}. We applied this approach to the rotation curve of a reference disk, LkCa 15, fitting the data both with and without the inclusion of substructures. Our results show that the most affected parameter is the scale radius, as it is directly influenced by the pressure gradient. However, the correction remains within the typical uncertainties. In contrast, the impact of substructures on the dynamical mass estimates is minimal.

3. Analysis

3.1. Sample

To apply this method, the crucial criteria are the availability of well-defined and precisely measured CO-emitting surfaces along which to appropriately sample the rotation curve, and the absence of nonaxisymmetric features, which may affect the azimuthal averaging, intrinsic to the definition of rotation curve, and the very assumption of centrifugal balance. This is important to ensure a correct extraction of the rotation curve, of the thermal structures and to evaluate at the right position (R, z) the model of Equation (5). Hence, it is not feasible to apply this method to the entire exoALMA sample. We discarded sources that show strong nonaxisymmetric features (MWC 758, CQ Tau) and low-inclination ones (HD 135344B, HD 143006, J1604), for which the extraction of the emitting layer is not well defined. Therefore, the sample used in this work includes AA Tau, DM Tau, HD 34282, J1615, J1842, J1852, LkCa 15, PDS 66, SY Cha, and V4046 Sgr.
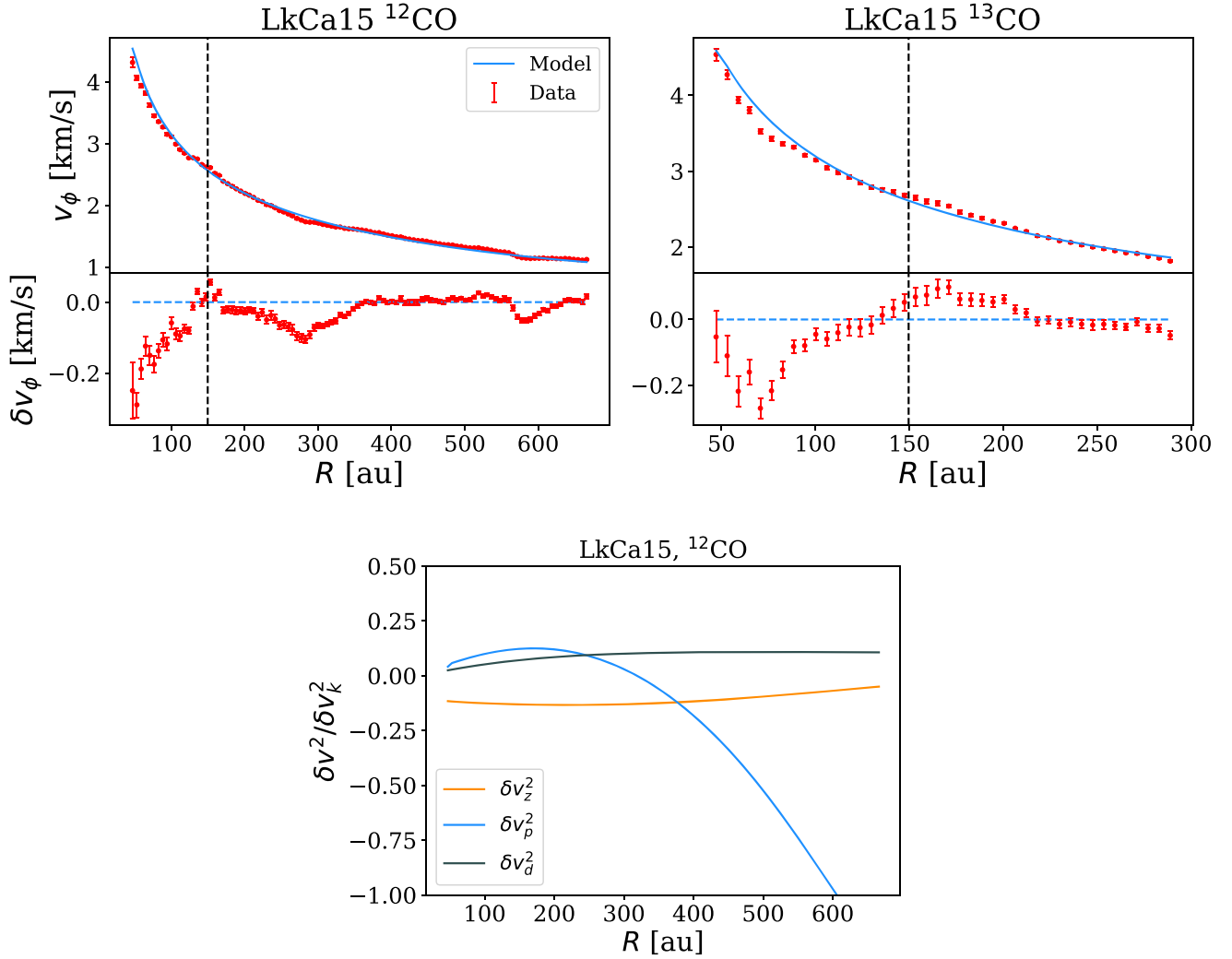
3.2. Rotation Curve Fits

The rotation curves used in this work have been extracted with DISCMINER and thoroughly discussed in J. Stadler et al. (2025) using the default cubes. The emitting layers of ^{12}CO and ^{13}CO are an output of DISCMINER as well. Finally, the thermal structure is extracted with DISKSURF and thoroughly discussed in M. Galloway-Sprietsma et al. (2025). The thermal and geometrical parameters are summarized in Appendix C. For each disk, both the ^{12}CO and ^{13}CO rotation curves are fitted simultaneously.

The rotation curve fits were performed using the code DYSC,[28] and the details can be found in Appendix B. All the DYSC fits were performed using 10 walkers, 5000 steps of burn-in steps, and 5000 steps. Initially, the walkers are uniformly distributed within their prior intervals. All the results are summarized in Table 1, where we present the best-fit values and their uncertainties, determined by the width of the posterior distributions. Hereafter, we will refer to the best-fit parameters obtained through this methodology as "dynamical values." Figure 1 shows the comparison between the data and the best-fit model for the ^{12}CO and ^{13}CO rotation curves for LkCa 15. The complete collection of comparison plots is shown in Appendix D. In our analysis, we excluded the first two major beam sizes in radius, as discussed in J. Stadler et al. (2025). The bottom panel of Figure 1 shows the non-Keplerian contributions to the rotation curve predicted by the best-fit model, where δv_z is the contribution given by the finite height of the emitting layer, δv_p is the pressure gradient contribution at the emitting layer, and δv_d is the self-gravitating contribution (G. Lodato et al. 2023).

When fitting AA Tau, we limited our analysis out to 250 au for the ^{12}CO since the outer part of the disk shows a drop in the nonparametric emitting height extracted by disksurf, as shown in M. Galloway-Sprietsma et al. (2025). This feature is also visible in the channel maps and in the rotation curve (see Appendix E) and leads to a systematic shift of the best-fit parameters since our model cannot take this into account. Despite excluding the outer region, the results for AA Tau still appear unusual, with the derived mass of the disk significantly high, marking AA Tau as an outlier in our sample. This is particularly clear when looking at the gas-to-dust ratio, at the percentage difference with the DISCMINER stellar mass and at α_S. This disk presents several atypical characteristics, and its anomalous behavior could be attributed to its high inclination, affecting the extraction of the emitting height and rotation curve, as suggested in M. Galloway-Sprietsma et al. (2025). While we include the results for completeness, they should be interpreted with caution due to these reasons.

---

[28] https://github.com/crislong/DySc

Figure 1. Top panels: rotation curves of LkCa 15 (red dots) with the best-fit model (blue lines) and residuals according to Equation (A13). The black dashed line represents the location of the scale radius R_c. Bottom panel: non-Keplerian contribution to the rotation curve, where δv_z is the correction due to the finite height of the emission, δv_p is the pressure gradient, and δv_d is the self-gravitating contribution.

Consequently, for the statistical analysis in this Letter, we exclude AA Tau from the sample and represent it in the figures with a cross rather than a square to denote its peculiar status.

The issue of the diffuse backside is also observed in SY Cha at $R > 400$ au and in the ^{13}CO data of LkCa 15 (M. Galloway-Sprietsma et al. 2025). We tested the robustness of the fits by including and excluding these regions, demonstrating that the results remain consistent for these disks.

3.3. Systematic Uncertainties

The EMCEE fitting procedure provides the uncertainties on the best-fit parameters but does not account for systematic errors. In particular, we model the pressure gradient contribution using the temperature structures presented in M. Galloway-Sprietsma et al. (2025). These temperature structures have their own uncertainties, which affect our results. To incorporate the systematic, we decided to run each EMCEE fit 100 times, drawing the thermal parameters from the posterior distribution of M. Galloway-Sprietsma et al. (2025). This procedure allows us to take the systematic errors driven by the thermal structure into account, returning a realistic uncertainty for the best-fit parameters, listed in Table 1.

In principle, the geometric parameters (inclination i and position angle PA) and the height of the emitting layer can contribute to the systematic uncertainties. However, the thermal structure dominates the systematic uncertainties since it directly impacts the pressure gradient characterization. Additionally, as pointed out in S. M. Andrews et al. (2024), the position of the center of the disk may induce significant uncertainties; for more information on how the center of the images is found we refer to A. Izquierdo et al. (2025) for the gas and P. Curone et al. (2025) for the continuum.

4. Results and Discussion

Before delving into the discussion of the results, we would like to emphasize that in Figures 2, 3, 4, and 5, different markers are used: orange squares represent exoALMA sources with a disk-to-star mass ratio[29] >5%, orange diamonds denote exoALMA sources with a disk-to-star mass ratio <5%, the orange cross marks AA Tau, and blue squares indicate the MAPS sources. The errors on MAPS sources are smaller compared to the exoALMA ones. This is because in P. Martire et al. (2024), the

---

[29] A disk-to-star mass ratio of 5% represents the lower limit for reliably measuring disk masses, as discussed by B. Veronesi et al. (2024) and S. M. Andrews et al. (2024).
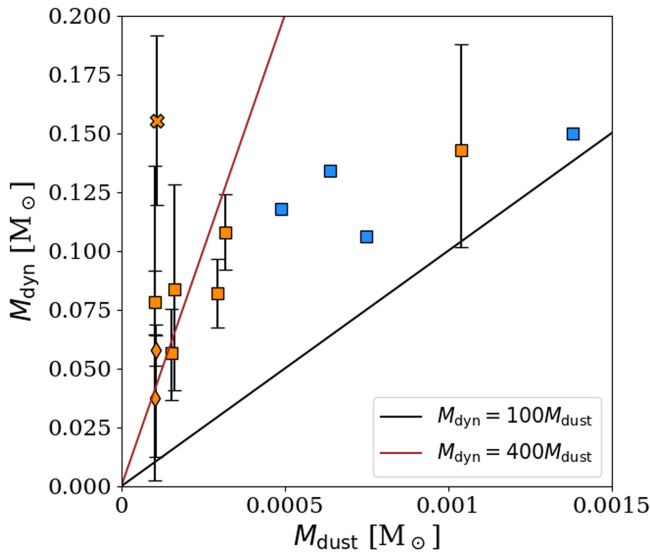
Figure 2. Dynamical masses against dust masses as computed in P. Curone et al. (2025) for the exoALMA and MAPS sources. The black line shows the $M_{\rm dyn} = 100 M_{\rm dust}$ and the brown line the $M_{\rm dyn} = 400 M_{\rm dust}$.

authors did not propagate the thermal structure uncertainties as we did in this work.

4.1. Stellar Masses

The best-fit values for the stellar masses are summarized in Table 1. The dynamical stellar masses generally deviate from the best-fit values provided by DISCMINER (A. Izquierdo et al. 2025; R. Teague et al. 2025). DISCMINER operates under the assumption that the azimuthal velocity is solely dictated by the stellar gravity, disregarding the pressure gradient and disk self-gravity. Consequently, the dynamical masses obtained in this work are a more accurate estimate, as all the relevant non-Keplerian contributions are considered.

In general, the pressure gradient has a decelerating effect on the azimuthal velocity,[30] leading to an underestimate of stellar mass when employing DISCMINER. Conversely, the contribution from the disk self-gravity increases the azimuthal velocity, causing an overestimate of the stellar mass. In Table 1, we observe that the combined effect of pressure gradient and self-gravity results in a discrepancy of a few percent in the stellar masses compared to the simple Keplerian fit model, as employed by DISCMINER, where we define $\Delta M = M_{\rm discminer} - M_{\rm dyn}$. In previous studies, dynamical masses were derived from low-resolution CO data and compared with pre-main-sequence evolutionary track predictions (M. Simon et al. 2000, 2017, 2019; T. A. M. Braun et al. 2021). However, due to the limited resolution of these data, the rotational profiles were approximated as Keplerian. Thanks to the high spatial and spectral resolution exoALMA data, we can now model the rotational profile more precisely, resulting in more accurate stellar mass estimates.

In general, excluding AA Tau as discussed before, we note that the percentage difference between dynamical masses and the DISCMINER ones is on the order of ~5%. We also note that

---

[30] The pressure gradient is always negative at the midplane, but this is not true at all (R, z). Indeed, it depends on how the emitting layer $z(R)$ relates to the disk hydrostatic structure. For instance, in a vertically isothermal disk, for $z \gtrsim 2H$, the pressure gradient is positive rather than negative. For more details about the vertical isothermal model, we refer to G. Lodato et al. (2023).

deviations go in both directions, showing that the combined contribution of self-gravity and pressure gradient is not easy to determine.

4.2. Disk Masses

The best-fit values for disk masses are presented in Table 1. As outlined by B. Veronesi et al. (2024) and S. M. Andrews et al. (2024), the minimum detectable disk-to-star mass ratio with this method is approximately 5%. In our sample, only three sources—J1852, PDS 66, and V4046—have best-fit disk mass values below this threshold. Table 1 lists all best-fit values, regardless of the disk mass detection threshold. In the following figures, these sources are marked with diamonds instead of squares to indicate that they fall below the measurability threshold. One can decide whether to employ the best-fit value we report or to use $M_d = 0.05 M_\star$ as an upper limit.
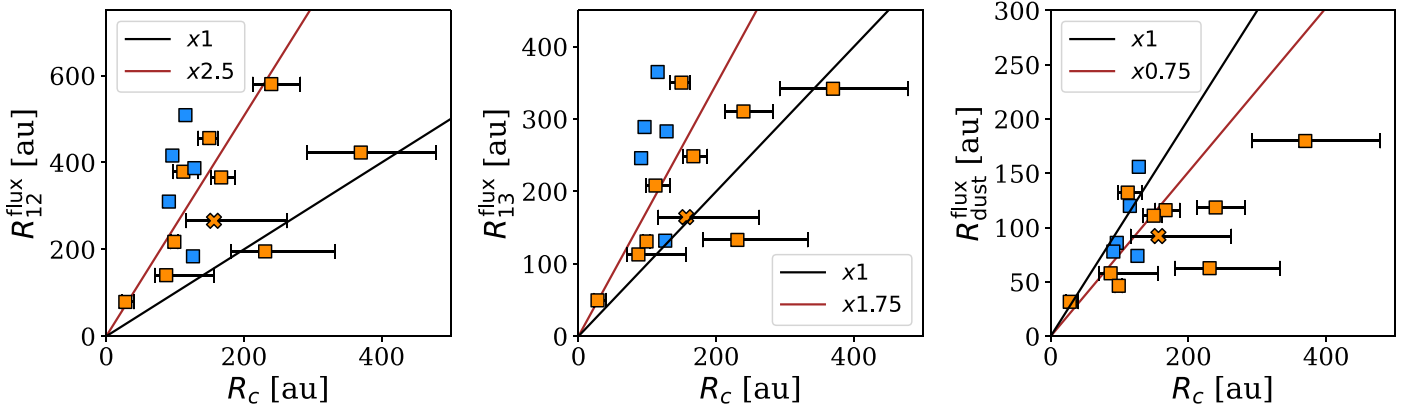
DM Tau, HD 34282, and LkCa 15 are the three sources whose disks have been independently estimated in the literature. In Figure 6, we compare the dynamical disk mass estimated in this Letter to these independent estimates.

For DM Tau, we estimated a dynamical mass of $M_d = 0.057^{+0.019}_{-0.020} M_\odot$. Its mass was estimated from the observation of hydrogen deuteride (HD) by M. K. McClure et al. (2016). For a chosen disk model, they determined the disk mass to be between $0.01 M_\odot$ and $0.047 M_\odot$. Hydrogen deuteride is a powerful molecule to determine disk mass since there is no chemistry involved, being an isotopologue of molecular hydrogen. L. Trapman et al. (2022) presented an innovative approach to measure protoplanetary disk masses using N_2H^+ and $C^{18}O$. This method enables the determination of the CO-to-H_2 mass ratio, facilitating the calibration of CO-based mass measurements (see A. Miotello et al. 2023; K. I. Öberg et al. 2023, for recent reviews). They applied this technique to DM Tau, determining that the disk mass lies between $0.031 M_\odot$ and $0.096 M_\odot$. To compare with the HD-based measurements of the disk mass, they repeated the analysis of M. K. McClure et al. (2016), but assuming a different disk structure, consistent with N_2H^+ models. They found a slightly higher HD-based disk mass between $0.04 M_\odot$ and $0.2 M_\odot$, which is the upper limit at the edge of gravitational instability. The value we obtained in our study is consistent with both N_2H^+ and HD-based measurements of L. Trapman et al. (2022).

For HD 34282, we estimated a dynamical mass of $M_d = 0.143^{+0.045}_{-0.041} M_\odot$. L. M. Stapper et al. (2024) constrained gas masses of Herbig disks using CO isotopologues, and HD 34282 is within their sample. Their estimate is $M_d = 0.12^{+0.19}_{-0.09} M_\odot$, perfectly consistent with our dynamical value.

For LkCa 15, we estimated a dynamical mass of $M_d = 0.108^{+0.016}_{-0.016} M_\odot$. S. Jin et al. (2019) constrained the gas and dust distribution in the LkCa 15 disk by comparing radiative transfer models with the ^{12}CO and dust emission from the Atacama Large Millimeter/submillimeter Array. They found that the best-fit value for the disk mass is $M_d = 0.1 M_\odot$, which reproduces the gas and dust emission very well. Conversely, J. A. Sturm et al. (2023) measured LkCa 15 gas mass using CO, ^{13}CO, $C^{18}O$, and $C^{17}O$ lines and modeled them with thermochemical models. They found that the gas mass in the LkCa 15 disk is $M_d = 0.01 M_\odot$, an order of magnitude smaller compared to the S. Jin et al. (2019) estimate. The main differences between the two methods lie in the assumptions about the disk structure, in particular in the disk surface density profile. Our estimate is consistent with S. Jin et al. (2019) and $\gtrsim 5\sigma$ inconsistent with J. A. Sturm et al. (2023).

Figure 3. Flux-based radii (i.e., radii enclosing 68% of the emission) of ^{12}CO, ^{13}CO, and dust compared with the dynamical scale radii R_c. The orange squares are the exoALMA sources, while the blue ones are the MAPS. The black line shows when the flux radius is equal to the dynamical one, and the brown line is the average value for the sources.
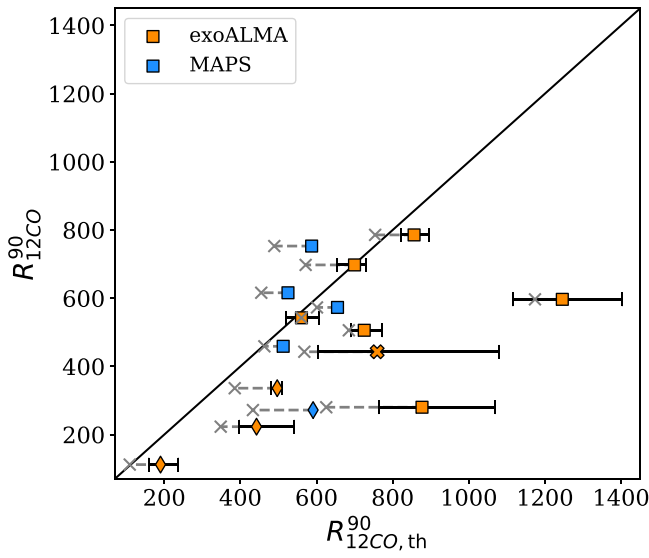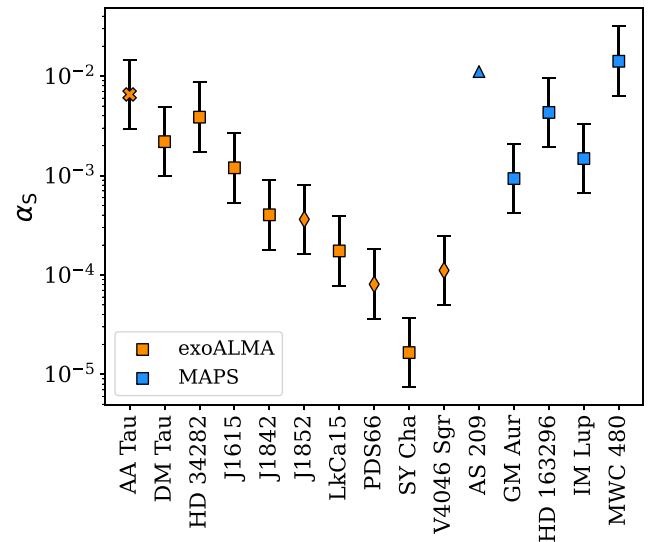

Figure 4. Comparison between the observed and the predicted radius enclosing the 90% of the ^{12}CO emission, according to Equation (9). The gray crosses show the results assuming the CO depletion obtained by L. Trapman et al. (2024).

Figure 5. α_S for the exoALMA and MAPS sources, computed according to Equation (10) and comparison with literature values.

PDS 66, or MP Mus, does not exhibit any substructure in dust continuum emission or gas, even at very high angular resolution $\Delta x = 0\rlap{.}{''}05$ (Á. Ribas et al. 2023), and in the rotation curves analyzed here there are no clear signs of pressure-induced substructures (L. M. Stapper et al. 2024). Á. Ribas et al. (2023) estimated the disk mass of PDS 66 by comparing the CO isotopologues' fluxes with models of J. P. Williams & W. M. J. Best (2014) and A. Miotello et al. (2016), showing that $M_d \simeq 10^{-4}–10^{-3} M_\odot$. Their estimate is consistent with our results, assuming $M_d/M_\star < 0.05$.

V4046 Sgr is a known spectroscopic binary with a period of 2.4 days and a mass ratio $q \simeq 0.94$ (H. C. Stempels & G. F. Gahm 2004). A. Miotello et al. (2016) presented chemical models to infer the disk mass from CO isotopologue emission. In that work, they gave an estimate of V4046 Sgr disk mass being $\sim 10^{-3} M_\odot$. The result is consistent when we assume the $M_d < 0.05 M_\star$ upper limit.
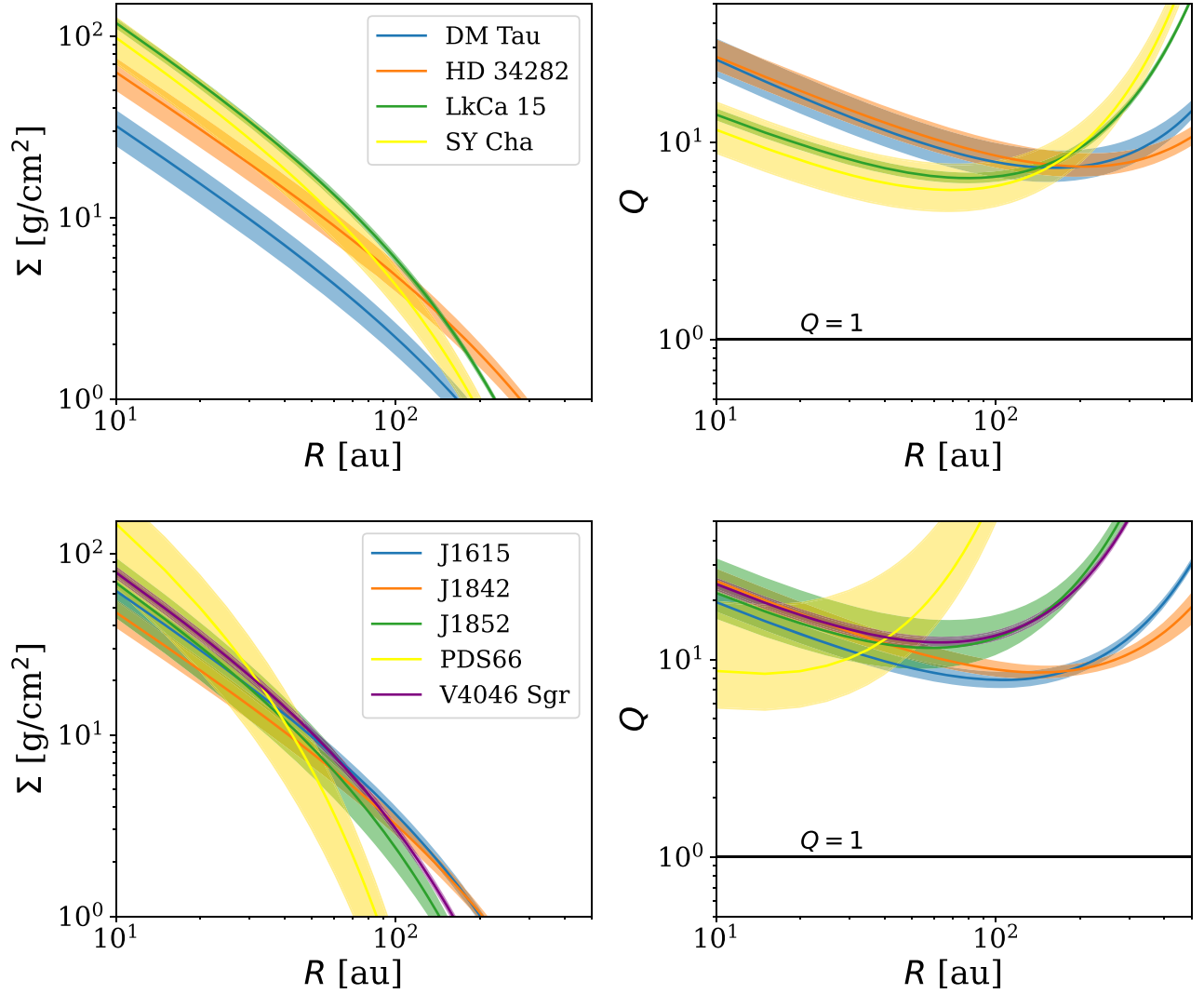
A comparison between dynamical masses and chemical masses obtained through the modeling of the N_2H^+ emission for the exoALMA sample is presented in L. Trapman et al. (2025).

Figure 6. Comparison between dynamical disk masses (this work) and literature estimates.

Figure 7. Top panel: surface density and Toomre Q profiles for the four most massive disks of our sample, namely, DM Tau, HD 34282, LkCa 15, and SY Cha, excluding AA Tau because of the big uncertainties (see Appendix E). Bottom panel: Surface density and Toomre Q profiles for the other five sources, namely, J1615, J1842, J1852, PDS 66, and V4046 Sgr.

4.2.1. Gas-to-dust Ratio

We use the fiducial values for the disk masses to compute the gas-to-dust ratio, employing the dust masses obtained by P. Curone et al. (2025). Table 1 presents the gas-to-dust ratios for the disks within the exoALMA sample, and Figure 2 shows the dynamical masses compared to the dust ones. The sources indicated with a diamond are the ones below the minimum disk mass threshold. Overall, the gas-to-dust ratios are above the standard value of 100, with an average value of ∼400. To compute the average gas-to-dust ratio, we have excluded AA Tau. It is not surprising that the inferred values are above 100. Indeed, dust masses computed in P. Curone et al. (2025) underestimate the total dust mass because of the optically thin emission hypothesis. Indeed, we expect the sources within the sample to be, at least, marginally optically thick in the inner parts. In addition, L. M. Stapper et al. (2024) estimated gas masses of Herbig disks and compared them with dust masses to obtain the gas-to-dust ratio. In their sample, they also observe a mean value of the gas-to-dust ratio of ∼400, as we find in this work. Interestingly, Figure 2 suggests that the gas-to-dust ratio is higher in low-dust-mass disks. These disks also tend to be

more compact, leading to higher optical depths, as it scales with the surface density.

4.2.2. Gravitational Instability?

To investigate the likelihood of a disk to be gravitationally unstable, we compute the Toomre Q parameter, defined as (A. Toomre 1964)

$$Q \simeq \frac{c_{s,\text{mid}}\Omega_k}{\pi G \Sigma} = 2\frac{H}{R}\bigg|_{\text{mid}}$$
$$\left(\frac{M_\star}{M_d}\right)\left(\frac{R}{R_c}\right)^{-1}\exp\left[\frac{R}{R_c}\right]. \tag{8}$$

This dimensionless parameter measures the strength of the stabilizing terms, pressure (c_s) and rotation (Ω_k), against the disk self-gravity (Σ). According to the Wentzel–Kramers–Brillouin quadratic dispersion relation (C. C. Lin & F. H. Shu 1964; A. Toomre 1964), the onset of the instability occurs when $Q \sim 1$. Figure 7 shows the surface density profiles and the Toomre parameter profiles for the disks within our sample. We are excluding AA Tau because of the large

uncertainties, and its case is thoroughly commented in Appendix E. The massive disks in our sample show $Q > 1$, meaning that they all are gravitationally stable. We underline that the temperature at the midplane is extrapolated from the 2D thermal structures (M. Galloway-Sprietsma et al. 2025).

4.3. Scale Radii

In this section, we discuss the relationship between the flux-based radii, i.e., the radii enclosing 68% of the ^{12}CO, ^{13}CO (M. Galloway-Sprietsma et al. 2025) and dust emission (P. Curone et al. 2025), and the scale radii R_c we find by modeling the rotation curve. As part of the discussion, we also add the MAPS sources. The masses and scale radii of the MAPS sources are taken from P. Martire et al. (2024), and the flux-based radii from C. J. Law et al. (2021). The flux-based gas and dust radii are reported in Table 2.

4.3.1. Gas-based Measurement

The left and the central panels of Figure 3 display the comparison between the dynamical and the flux-based radii of ^{12}CO and ^{13}CO. As expected, the flux-based radii are larger compared to the dynamical scale radius, showing an average ratio of 2.5 for the ^{12}CO and 1.75 for the ^{13}CO. However, R_c is a crucial quantity in the context of protoplanetary disk evolution, as it relates to the disk's lifetime and the efficiency of radial drift. The relationship between the flux-based radii and R_c is complex, involving thermochemical information and potentially depending on the sensitivity of the observations. This issue was addressed by C. Toci et al. (2023) and L. Trapman et al. (2023), who found a relationship between R_{12CO}^{90} and R_c and M_d, which reads

$$R_{12CO,theor}^{90} = R_c \mathcal{W}\left[4.9 \times 10^7 \left(\frac{M_d}{M_\odot}\right)^{0.66}\left(\frac{R_c}{au}\right)^{-2}\right], \quad (9)$$

where $\mathcal{W}$ is the Lambert function. This expression assumes a CO abundance that typically is considered to be $X_{CO} = 10^{-4}$, and this information is enclosed into the constant 4.9×10^7. Figure 4 shows the comparison between the radius enclosing 90% of the ^{12}CO emission and the theoretical expectation according to Equation (9). The error bars take into account the uncertainty on the disk mass and scale radius. We observe that the theoretical expectations systematically overestimate the CO radius. A possible explanation is CO depletion. L. Trapman et al. (2023) obtain Equation (9) using thermochemical models, fixing the CO abundance at $X_{CO} = 10^{-4}$. There, the dependence on CO abundance is not explicitly stated. Assuming a linear relationship between the CO abundance and the argument of the Lambert function in Equation (9), as done in C. Toci et al. (2023), we see that reducing the CO abundance brings the theoretical values closer to the observed ones. G. Rosotti et al. (2025) and L. Trapman et al. (2025) provided two distinct inferences of CO depletion for the exoALMA sample. G. Rosotti et al. (2025) derived the CO depletion required to reconcile their estimated disk masses with the dynamical values presented in this Letter, meaning their method is not entirely independent of our estimates. In contrast, L. Trapman et al. (2025) presented an independent estimate of CO depletion by forward-modeling N_2H^+ and rare CO

Table 2
Flux-based Radii of Dust, ^{12}CO, and ^{13}CO Emission for the exoALMA and MAPS Sources (C. J. Law et al. 2021; M. Galloway-Sprietsma et al. 2025)

Source	R_d^{68} (au)	R_{12CO}^{68} (au)	R_{13CO}^{68} (au)
AA Tau	92	265	164
DM Tau	119	580	310
HD 34282	180	422	341
J1615	116	365	248
J1842	63	195	133
J1852	58	140	113
LkCa 15	111	457	351
PDS 66	32	108	50
SY Cha	132	376	207
V4046 Sgr	46	216	130
AS 209	74	184	132
GM Aur	86	416	289
HD 163296	78	310	246
IM Lup	120	509	365
MWC 480	156	387	283

isotopologue emission in the exoALMA disks. Both studies consistently indicate that CO depletion is needed, aligning with the discrepancy we report. The gray crosses in Figure 3 represent the values of R_{CO} calculated using the CO abundance derived by L. Trapman et al. (2025). For most of the sources, using these CO abundances results in a better agreement with the observed values.

4.3.2. Dust-based Measurement

The right panel of Figure 3 displays the comparison between the dynamical and the flux-based radius of dust emission. On average, the dust radii are smaller than the scale radii, showing an average ratio of 0.75. This trend is expected because, beyond R_c, the surface density profile is exponentially tapered, enhancing the effect of radial drift (T. Birnstiel & S. M. Andrews 2014).

C. Toci et al. (2021) presented theoretical models of protoplanetary disk evolution influenced by viscosity, grain growth, and radial drift and studied the ratio between the scale radius and the dust. They found that the expected ratio between the scale and dust radii should be $\gtrsim 5$, significantly larger than the average ratios measured in our samples. One possible reason may be the role of substructures, that slow down radial drift. Indeed, all the disks, except for PDS 66, show substructures in dust continuum emission; for a detailed characterization of dust substructures, we refer to P. Curone et al. (2025).

4.4. Transport of Angular Momentum—Effective α_S

We modeled the disks in the exoALMA sample under the assumption of a self-similar surface density distribution. This approach allowed us to fit the stellar mass, disk mass, and scale radius using the rotation curves of CO isotopologues. Consequently, we now have a comprehensive picture of the disks' structure, enabling us to study their evolution within a viscous framework (N. I. Shakura & R. A. Sunyaev 1973), introducing an effective viscous parameter α_S. Indeed, the self-similar hypothesis establishes relationships between disk properties such as temperature, mass, size, and α_S with the accretion rate onto the central object. By measuring the

Table 3
Accretion Rate and α_S for the exoALMA and MAPS Sources

Source	$\log_{10} \dot{M}_\star \, [M_\odot \, \mathrm{yr}^{-1}]$	$\dot{M}_\star$ References	α_S	Literature Values	References
AA Tau	-7.35 ± 0.35	C. F. Manara et al. (2023)	$6.54^{+8.11}_{-3.62} \times 10^{-3}$	...	...
DM Tau	-8.2 ± 0.35	C. F. Manara et al. (2014)	$2.19^{+2.72}_{-1.21} \times 10^{-3}$	0.08 ± 0.02	K. Flaherty et al. (2020)
HD 34282	-7.69 ± 0.35	J. R. Fairlamb et al. (2015)	$3.86^{+4.79}_{-2.14} \times 10^{-3}$	...	...
J1615	-8.25 ± 0.35	C. F. Manara et al. (2014)	$1.20^{+1.48}_{-0.66} \times 10^{-3}$	...	...
J1842	-8.8 ± 0.35	C. F. Manara et al. (2014)	$4.03^{+4.99}_{-2.23} \times 10^{-4}$	...	...
J1852	-8.7 ± 0.35	C. F. Manara et al. (2014)	$3.62^{+4.49}_{-2.01} \times 10^{-4}$	...	...
LkCa 15	-8.7 ± 0.35	C. F. Manara et al. (2014)	$1.74^{+2.16}_{-0.97} \times 10^{-4}$	...	...
PDS 66	-9.18 ± 0.35	L. Ingleby et al. (2013)	$8.06^{+9.99}_{-4.46} \times 10^{-5}$	...	...
SY Cha	-9.89 ± 0.35	C. F. Manara et al. (2023)	$1.66^{+2.05}_{-0.92} \times 10^{-5}$	...	...
V4046 Sgr	-9.3 ± 0.35	J. F. Donati et al. (2011)	$1.11^{+1.38}_{-0.61} \times 10^{-4}$	<0.014	K. Flaherty et al. (2020)
AS 209	-7.3 ± 0.35	K. I. Öberg et al. (2021)	$> 1.11 \times 10^{-2}$	...	...
GM Aur	-8.1 ± 0.35	K. I. Öberg et al. (2021)	$9.32^{+11.1}_{-5.16} \times 10^{-4}$	...	...
HD 163296	-7.4 ± 0.35	K. I. Öberg et al. (2021)	$4.31^{+5.35}_{-2.38} \times 10^{-3}$	<0.003	K. M. Flaherty et al. (2015, 2017)
IM Lup	-7.9 ± 0.35	K. I. Öberg et al. (2021)	$1.48^{+1.18}_{-0.82} \times 10^{-3}$	$3.0^{+0.4}_{-0.9} \times 10^{-3}$	R. Franceschi et al. (2023)
				$0.25^{+0.09}_{-0.09}$	T. Paneque-Carreño et al. (2024)
				$5.76^{+8.68}_{-2.52} \times 10^{-2}$	K. Flaherty et al. (2024)
MWC 480	-6.9 ± 0.35	K. I. Öberg et al. (2021)	$1.41^{+1.17}_{-0.78} \times 10^{-2}$	<0.006	K. Flaherty et al. (2020)

Note. The literature values for α_S are based on different methods, mainly line broadening.

accretion rates, we can, in principle, constrain the instantaneous α_S using (i.e., L. Hartmann 1998)

$$\alpha_S = \frac{2}{3} \frac{\dot{M}_\star}{M_d \Omega_c} \left(\frac{H_c}{R_c} \right)^{-2}, \qquad (10)$$

where the subscript c denotes that the corresponding quantity is evaluated at the scale radius.

The reader should remember that α_S was introduced to explain why disks accrete, and it is not a viscosity theory. Therefore, the correct interpretation of the formula above is the effective value of α_S needed to reproduce the observed accretion rate. Additionally, the formula does not imply that accretion is driven by turbulence; the values it returns should be interpreted as an effective α_S, i.e., the amount of transported angular momentum. Any mechanism proposed to explain angular momentum transport in disks would need to exhibit an equivalent efficiency of angular momentum transport, even MHD winds (B. Tabone et al. 2022). We point out that here we are assuming that stellar accretion, which happens in the <1 au region of the disk, is equal to the disk accretion, measured at the scale radius.

Several studies tackled this problem in the past (S. M. Andrews et al. 2009, 2010; R. R. Rafikov 2017; M. Ansdell et al. 2018; N. van der Marel et al. 2021), showing that $\alpha_S > 10^{-4}$ is needed to explain the observed accretion rate. However, disk masses were estimated through dust emission, and the scale radius was modeled from dust emission or interpreted as a fixed fraction of the ^{12}CO spectral line flux. Here, we are able to correctly determine the α_S needed to explain accretion since we have a dynamical disk mass estimate and a good measurement of the scale radius.

Figure 5 presents the values of α_S calculated using Equation (10) for the exoALMA and MAPS sources. In the exoALMA sample, the diamonds represent the disk with a disk mass below measurable threshold, and for AS 209, we use $M_d = 0.05 M_\star$ as an upper limit, as commented in P. Martire et al. (2024). Table 3 provides the detailed values along with their associated uncertainties. The determination of α_S involves two primary sources of error: the uncertainties related to the

accretion rate and the parameters of the disk. Our analysis indicates that the uncertainties in α_S are predominantly influenced by the uncertainties in the accretion rate, $\dot{M}_\star$. As reported by C. F. Manara et al. (2023), the fractional uncertainty in individual accretion rate measurements at any given time is approximately 0.35 dex, a value that we have adopted for our analysis. Overall, the effective α_S we obtain is $>10^{-5}$ in all cases and $>10^{-4}$ in most cases. What is peculiar in Figure 5 is that the range of α_S is broad, from 10^{-5} to 10^{-2}, possibly pointing to different mechanisms driving angular momentum transport or even accretion rate variability.

For five sources within our sample, namely, DM Tau, V4046 Sgr, MWC 480, IM Lup and HD 163296, there are independent α_S constraints, obtained by modeling the nonthermal molecular line broadening (K. M. Flaherty et al. 2015, 2017; K. Flaherty et al. 2020) or by determining the dust emission radial profile with radiative transfer models (R. Franceschi et al. 2023). The literature values are listed in Table 3.

The case of DM Tau is particularly interesting since the two estimates disagree by 2 orders of magnitude, with our value pointing toward a lower viscosity $\alpha \sim 10^{-3}$. To model the nonthermal line broadening in DM Tau, K. Flaherty et al. (2020) assume a stellar mass of $M_\star = 0.54 M_\odot$, which differs by $\sim 20\%$ from our best-fit value $M_\star = 0.456 M_\odot$. This difference in stellar mass could explain the inconsistency between the α-values; indeed, the lower the stellar mass, the bigger the iso-velocity region for a fixed velocity interval Δv.

As for V4046 Sgr, our lower value is in agreement with K. Flaherty et al. (2020) upper value, pointing to $\alpha \in (10^{-4}, 10^{-2})$. For the MAPS sources MWC 480 and HD 163296, our estimate is in overall good agreement with K. M. Flaherty et al. (2017) and K. Flaherty et al. (2020) upper limits. Finally, for IM Lup R. Franceschi et al. (2023) modeled dust emission with different α_S values, post-processed the models with radiative transfer codes and compared them with the actual data. They found that an α_S of 3×10^{-3} best reproduces the data. Their estimate agrees with our value within the uncertainties. By contrast, T. Paneque-Carreño et al. (2024) estimated the viscosity through the characterization of

CN and C_2H. Leveraging on the optical depth properties of these two tracers, they measured the turbulence from the nonthermal broadening of the line at the location of the emitting layer. Recently, K. Flaherty et al. (2024) also estimated α for IM Lup by the molecular line broadening model, showing a good agreement with T. Paneque-Carreño et al. (2024). They found a high value of viscosity, almost 2 orders of magnitude higher compared to our estimate and the R. Franceschi et al. (2023) one, pointing to a vertical gradient of α, as expected from instabilities like the magnetorotational instability.

5. Conclusions

High-resolution rotation curves of protoplanetary disks can be used to constrain fundamental disk properties, namely, the stellar mass, the disk mass, and the scale radius. In this work, we analyzed rotation curves of ^{12}CO and ^{13}CO for the exoALMA sources to infer these parameters. Here, we summarize our findings

1. We constrained the dynamical disk mass for 10 sources within the exoALMA sample. Combined with the results from P. Martire et al. (2024) and B. Veronesi et al. (2021), this brings the total number of dynamical disk mass estimates to 16. This method is independent of assumptions about disk chemical composition and does not rely on any specific tracer. Among the 10 sources analyzed in the exoALMA sample, 7 exhibit a disk-to-star mass ratio exceeding 5%. We evaluated the Toomre parameter to assess gravitational stability and found that all sources are gravitationally stable, consistent with the absence of prominent spiral structures.

2. We compared the dynamical disk masses with the dust-based ones (P. Curone et al. 2025), with the assumption of optically thin continuum emission, to determine the gas-to-dust ratio. We found values consistently above the standard 100, with an average of approximately 400. These large ratios likely result from the underestimation of dust masses due to the assumption of optically thin emission.

3. Thoroughly modeling the pressure gradient contribution allows for an accurate estimation of the scale radius R_c. We compared the scale radius estimates with flux-based measurements for CO isotopologues and dust, finding that the dust continuum emission radii are comparable to R_c. This suggests that pressure-modulated substructures may mitigate radial drift. Additionally, we find that the gas-based radii are consistently larger than R_c. Using the derived R_c and M_d, we calculated the theoretical flux-based CO radii (L. Trapman et al. 2023) and compared them with the observed values. The theoretical predictions systematically overestimate the CO radii, possibly indicating CO depletion. We recomputed the CO radii using the CO depletion factor derived by L. Trapman et al. (2025) through forward-modeling N_2H^+ and $C^{18}O$ emissions. For most of the sources, this results in a better agreement.

4. Correctly modeling the non-Keplerian contributions to the rotation curves allows for precise estimates of stellar masses. The dynamical stellar masses, which incorporate the effects of pressure gradients and disk self-gravity, provide a more accurate estimate of this quantity compared to simple Keplerian models, as shown in P. Martire et al. (2024) and S. M. Andrews et al. (2024).

5. The knowledge of M_d, $M_\star$, and R_c allows us to investigate protoplanetary disk evolution, particularly the transport of angular momentum within an α_S description. Our results show that the effective α_S for the disks is generally $>10^{-5}$, with statistical uncertainties driven primarily by the accretion rate measurements.

Appendix A
Model for the Rotation Curve

In this paragraph, we summarize the main findings of G. Lodato et al. (2023) and P. Martire et al. (2024).

Although the calculations are valid for an arbitrary surface density Σ, in this work we assume that it is described by the self-similar solution of D. Lynden-Bell & J. E. Pringle (1974)

$$\Sigma(R) = \frac{(2-\gamma)M_d}{2\pi R_c^2}\left(\frac{R}{R_c}\right)^{-\gamma}\exp\left[-\left(\frac{R}{R_c}\right)^{2-\gamma}\right], \quad (A1)$$

where M_d and R_c are the disk mass and the scale radius respectively, R is the cylindrical radius and γ describes the steepness of the surface density, and we adopt $\gamma = 1$.

The disk density at the midplane ρ_{mid} is

$$\rho_{\mathrm{mid}} \propto \frac{\Sigma}{H_{\mathrm{mid}}} \propto R^{-(\gamma+(3-q_{\mathrm{mid}})/2)}\exp\left[-\left(\frac{R}{R_c}\right)^{2-\gamma}\right], \quad (A2)$$

where

$$H_{\mathrm{mid}} = c_{s,\mathrm{mid}}/\Omega_k, \quad (A3)$$

is the disk hydrostatic height at the midplane,

$$c_{s,\mathrm{mid}} = \sqrt{k_b T_{\mathrm{mid}}/(\mu m_p)} \propto R^{-q_{\mathrm{mid}}/2} \quad (A4)$$

is the sound speed at the disk midplane, k_b is the Boltzmann constant, μ is the mean molecular weight, usually assumed to be 2.35, m_p the proton mass and

$$\Omega_k = \sqrt{GM_\star/R^3} \quad (A5)$$

is the Keplerian frequency.

We take into account that protoplanetary disks are thermally stratified by defining a function f that describes how the temperature changes vertically

$$\begin{aligned} T(R, z) &= T_{\mathrm{mid}}(R)f(R, z) \\ c_s^2(R, z) &= c_{s,\mathrm{mid}}^2(R)f(R, z). \end{aligned} \quad (A6)$$

In this work, we will use Equation (1) as $f(R, z)$. Also, the density has a vertical dependence, which we describe as

$$\rho(R, z) = \rho_{\mathrm{mid}}(R)g(R, z), \quad (A7)$$

where the value of $g(R, z)$ is linked to $f(R, z)$ through hydrostatic equilibrium. Finally, the pressure P is described as

$$P(R, z) = P_{\mathrm{mid}}(R)fg(R, z) = c_{s,\mathrm{mid}}^2(R)\rho_{\mathrm{mid}}(R)fg(R, z). \quad (A8)$$

As shown in P. Martire et al. (2024), from the hydrostatic equilibrium the relationship between f and g is

$$\log(fg) = -\frac{1}{H_{\mathrm{mid}}^2}\int_0^z \frac{z'}{f}\left[1 + \left(\frac{z'}{R}\right)^2\right]^{-3/2}dz'. \quad (A9)$$

Hence, the density structure is

$$\rho(R, z) = \frac{\rho_{\mathrm{mid}}(R)}{f(R,z)}$$
$$\exp\left\{-\frac{1}{H_{\mathrm{mid}}^2}\int_0^z \frac{z'}{f(z',R)}\left[1 + \left(\frac{z'}{R}\right)^2\right]^{-3/2}dz'\right\}, \quad (A10)$$

which, in the isothermal case ($f = 1$), reduces to

$$\rho(R, z) = \rho_{\mathrm{mid}}(R)\exp\left[-\frac{R^2}{H_{\mathrm{mid}}^2}\left(1 - \frac{1}{\sqrt{1 + z^2/R^2}}\right)\right], \quad (A11)$$

which, for $z << R$, reduces to the standard Gaussian profile often used to approximate the disk vertical structure. Assuming the condition of centrifugal balance, the rotation curve is given by the radial component of the Navier–Stokes equation

$$v_\phi^2(R, z) = \frac{R}{\rho}\frac{dP}{dR}(R, z) + R\frac{d\Phi_\star}{dR}(R, z) + R\frac{d\Phi_d}{dR}(R, z), \quad (A12)$$

where $\Phi_\star$ is the stellar gravitational potential and Φ_d is the disk one. Expanding Equation (A12), we obtain

$$v_\phi^2 = v_k^2\left\{\left[1 + \left(\frac{z}{R}\right)^2\right]^{-3/2} - \left[\gamma' + (2-\gamma)\left(\frac{R}{R_c}\right)^{2-\gamma} - \right.\right.$$
$$\left.\left. - \frac{d\log(fg)}{d\log R}\right]\left(\frac{H}{R}\right)_{\mathrm{mid}}^2 f(R, z)\right\} + v_d^2, \quad (A13)$$

where $\gamma' = \gamma + (3 + q_{\mathrm{mid}})/2$, $v_k = \Omega_k R$ and

$$v_d^2 = G\int_0^\infty \left[K(k) - \frac{1}{4}\left(\frac{k^2}{1-k^2}\right)\right.$$
$$\left. \times \left(\frac{R'}{R} - \frac{R}{r} + \frac{z^2}{RR'}\right)E(k)\right]\sqrt{\frac{R'}{R}}k\Sigma(R')dR', \quad (A14)$$

where $K(k)$ and $E(k)$ are complete elliptic integrals (M. Abramowitz & I. A. Stegun 1970) and $k^2 = 4RR'/[(R + R')^2 + z^2]$.

Appendix B
DySc Code and Statistical Framework

We implemented the fitting procedure for the stellar mass, disk mass, and scale radius based on the model of Equation (A13) in the code DYSC,[31] already used in G. Lodato et al. (2023) and P. Martire et al. (2024). The code implements Markov Chain Monte Carlo through the EMCEE library (D. Foreman-Mackey et al. 2013). According to Bayes

---

[31] https://github.com/crislong/DySc

theorem, the probability of the parameters $\theta_i = [M_\star, M_d, R_c]$, given the data v with their error σ_v, and under the assumption of the model H (i.e., the posterior probability $\mathcal{P}$), can be expressed as

$$P(\theta_i | v; H) = \frac{P(v; H|\theta_i)P(\theta_i)}{P(v)} = \frac{P(v; H|\theta_i)P(\theta_i)}{\int d\theta_i P(v|\theta_i)P(\theta_i)}, \quad (B1)$$

where $P(v|\theta) = \mathcal{L}$ is the likelihood, $P(\theta_i)$ denotes the priors and $P(v) = \mathcal{E}$ is the evidence. For computational reasons, it is more convenient to work with the logarithm of the probability functions. Hence, the Bayes theorem becomes

$$\log \mathcal{P} = \log \mathcal{L} + \log P(\theta_i) - \log \mathcal{E}. \quad (B2)$$

The logarithm of the likelihood we choose is

$$\log \mathcal{L} = -\frac{N}{2} \sum_i^N \log(2\pi\sigma_{v,i}) - \frac{1}{2\sigma_{v,i}^2}(v_i^{\text{data}} - v_i^{\text{model}})^2. \quad (B3)$$

Here, we make the standard assumption that the data are distributed around the true value following a Gaussian distribution, with standard deviation σ_v, and that they are not correlated. Although this is not entirely true because of the finite beam size and the rotation curve extraction procedure, quantifying the correlation between the data is beyond the scope of the Letter. The chosen priors for the model parameters are uniform distributions respectively centered on $M_\star \in \mathcal{U}[0, 5]M_\odot$, $M_d \in \mathcal{U}[0, 1]M_\odot$, and $R_c \in \mathcal{U}[10, 1000]$ au, where the lower limit for the prior is justified by the angular resolution.

All the fits are performed fixing the power law coefficient of the surface density $\gamma = 1$, underestimating the true uncertainties. In addition, this choice introduces a potential bias on the scale radius, which is the parameter most affected by the choice of γ, while the disk and stellar masses are not (S. M. Andrews et al. 2024).

Appendix C
Geometrical and Thermal Parameters of the Sources

Tables 4 and 5 show the emitting layer and the thermal parameters used for the fitting procedure, respectively. The heights of the emitting layers have been obtained with DISCMINER (A. Izquierdo et al. 2025) and the thermal parameters with DISKSURF (M. Galloway-Sprietsma et al. 2025).

Table 4
Height of the Emitting Layers Extracted with DISCMINER (A. Izquierdo et al. 2025) and Used in the Fitting Procedure in This Work

| Source	i (deg)	Line	z_0 (au)	ψ	r_t (au)	q_t
AA Tau	58.7	^{12}CO $J = 3$–2	49.8	1.2	240.1	1.35
		^{13}CO $J = 3$–2	51.7	1.36	151.2	1.35
DM Tau	38.7	^{12}CO $J = 3$–2	86.6	1.87	79.6	0.48
		^{13}CO $J = 3$–2	19.7	2.27	241.7	0.93
HD 34282	58.3	^{12}CO $J = 3$–2	34.0	1.19	512.2	3.2
		^{13}CO $J = 3$–2	27.2	0.79	509.9	4.41
J1615	46.5	^{12}CO $J = 3$–2	26.3	1.04	529.6	6.89
		^{13}CO $J = 3$–2	19.0	1.04	424.8	5.92
J1842	39.4	^{12}CO $J = 3$–2	25.9	1.46	210.6	1.89
		^{13}CO $J = 3$–2	17.5	1.7	143.4	2.01
J1852	32.7	^{12}CO $J = 3$–2	75.3	1.78	60.9	0.84
		^{13}CO $J = 3$–2	31.2	2.74	90.3	1.33
LkCa 15	50.3	^{12}CO $J = 3$–2	29.0	1.06	795.3	3.19
		^{13}CO $J = 3$–2	27.3	0.87	511.0	3.46
PDS 66	31.9	^{12}CO $J = 3$–2	17.4	1.83	127.0	4.48
		^{13}CO $J = 3$–2	7.5	1.2	29.0	1.54
SY Cha	52.4	^{12}CO $J = 3$–2	43.3	1.79	209.8	1.02
		^{13}CO $J = 3$–2	72.9	2.44	66.1	0.7
V4046 Sgr	34.1	^{12}CO $J = 3$–2	25.8	1.84	151.2	1.17
		^{13}CO $J = 3$–2	33.5	1.57	65.6	1.14

Table 5
2D Temperature Structure Fits from M. Galloway-Sprietsma et al. (2025) Using the Dartois Prescription of Equation (1)

| Source	$T_{\text{atm,100}}$ (K)	$T_{\text{mid,100}}$ (K)	q_{atm}	q_{mid}	Z_0 (arcsec)	β
AA Tau	41	13	-0.51	-0.21	0.45	0.07
DM Tau	37	20	-0.46	-0.37	0.16	0.0
HD 34282	67	32	-0.0	-0.25	0.28	0.69
J1615	34	24	-0.1	-0.25	0.21	1.11
J1842	43	25	-0.45	-0.23	0.18	0.0
J1852	40	30	-0.87	-0.37	0.11	0.0
LkCa 15	48	20	-0.55	-0.23	0.35	0.59
PDS 66	38	31	0	-0.08	0.11	1.21
SY Cha	45	24	-0.58	-0.3	0.31	0.01
V4046 Sgr	37	28	-0.63	-0.35	0.14	0.0

## Appendix D
Best-fit Models and Corner Plots

Figures 8, 9, and 10 show the best-fit rotation curves with the model residuals. Figures 11, 12, and 13 show the corner plots and the posterior distributions for the stellar mass, disk mass, and scale radius.
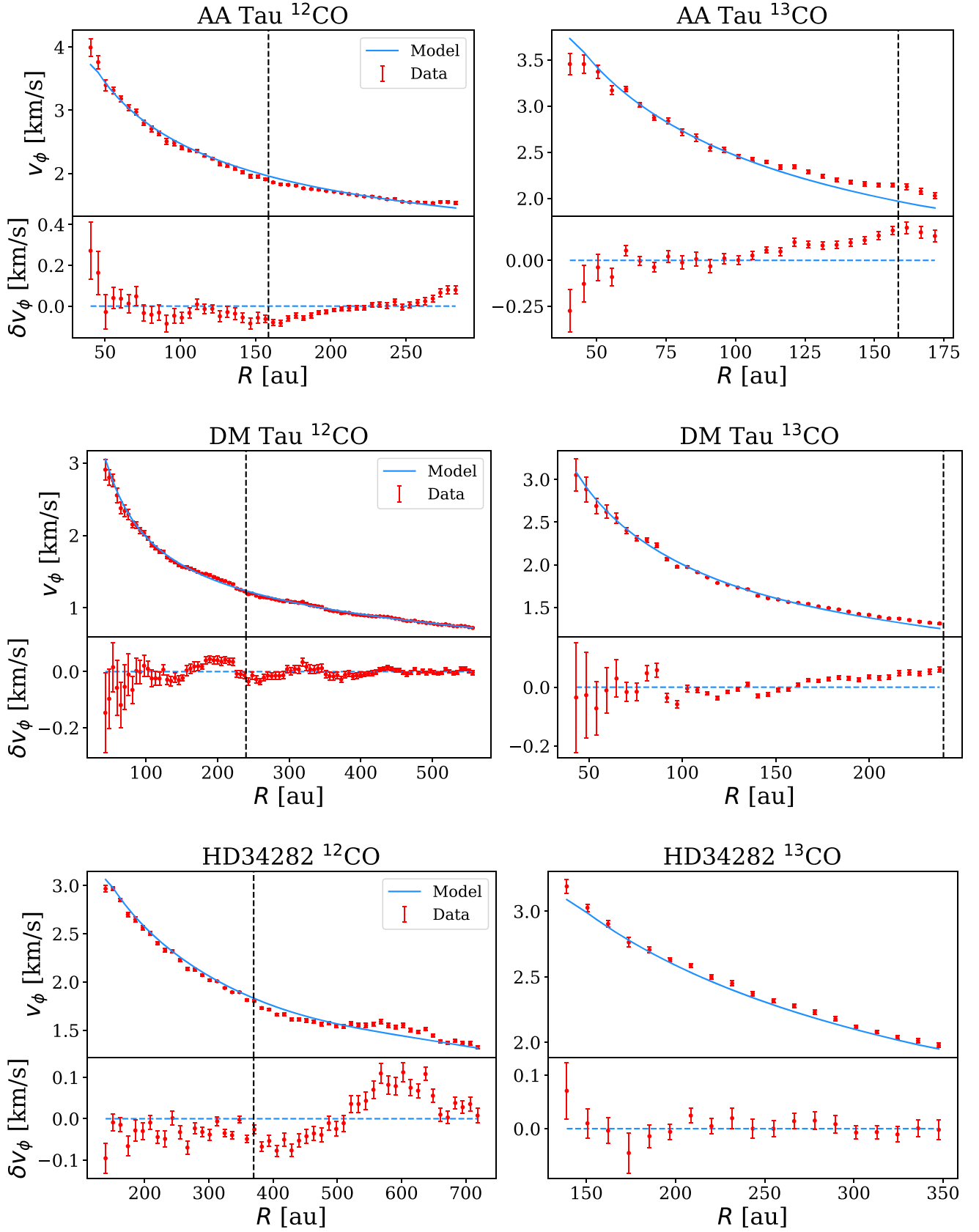
Figure 8. Rotation curve of the disks within our sample (red dots) of the ^{12}CO (left panels) and ^{13}CO (right panels) with the best-fit model using Equation (A13).
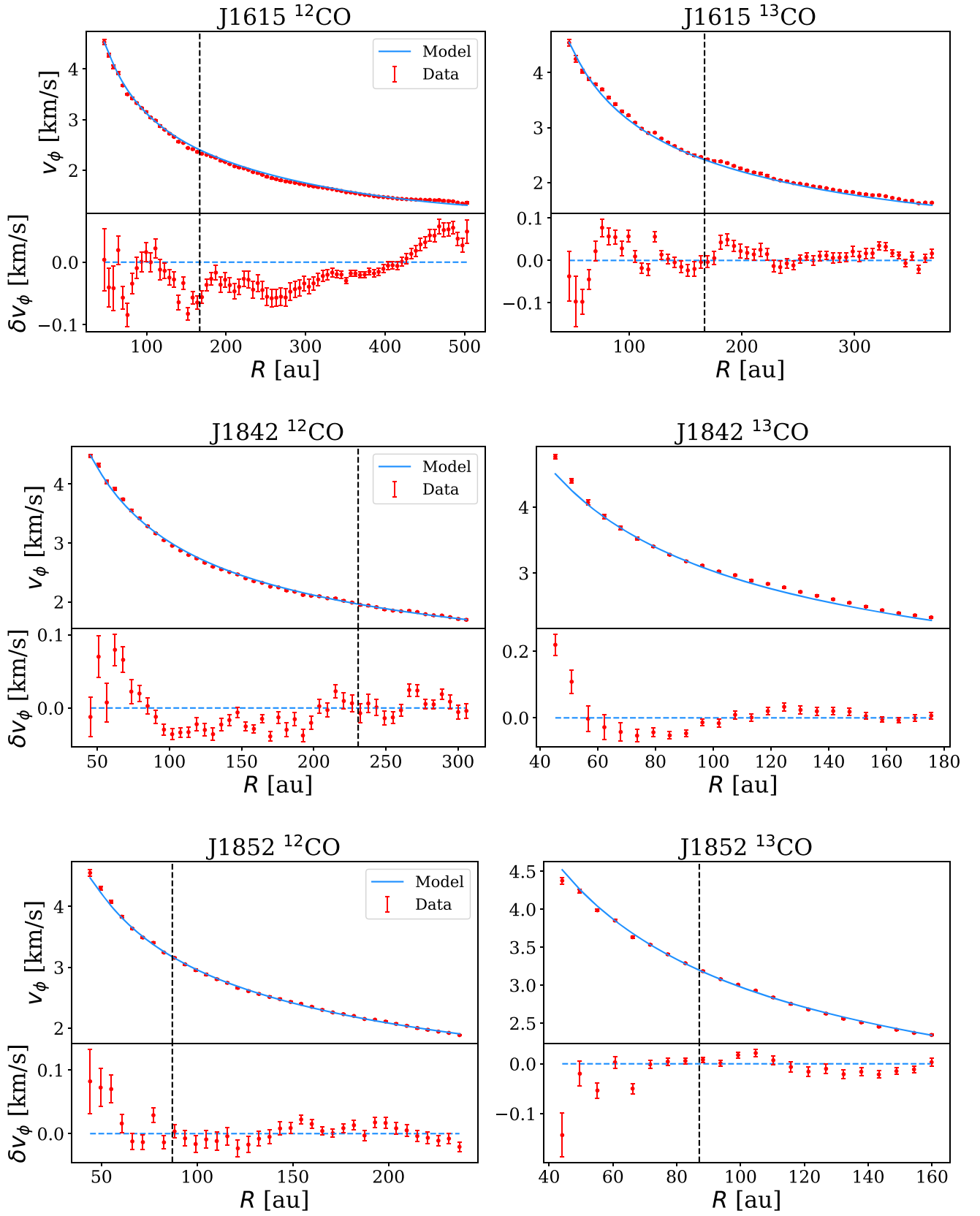
Figure 9. Rotation curve of the disks within our sample (red dots) of the ^{12}CO (left panels) and ^{13}CO (right panels) with the best-fit model using Equation (A13).
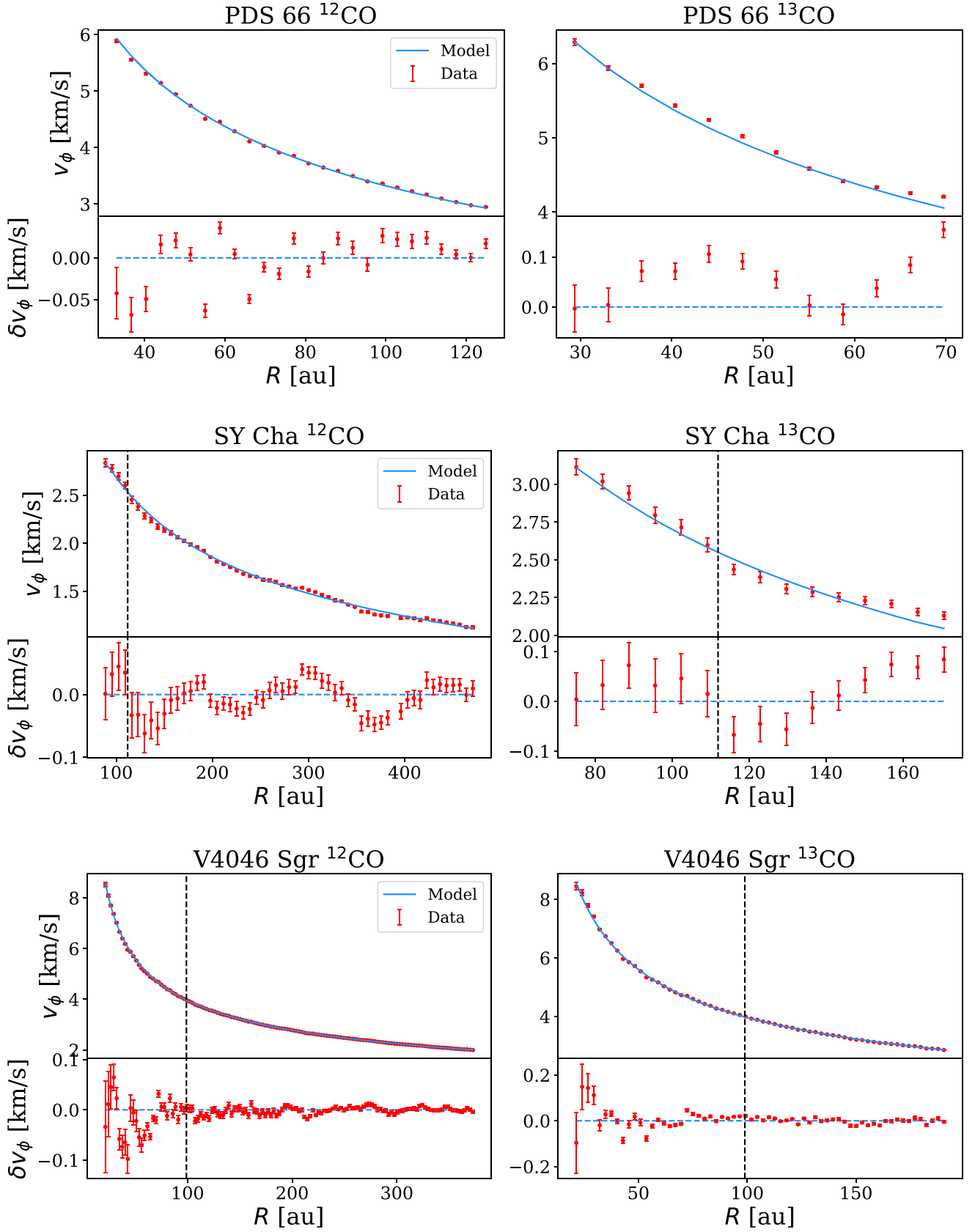
Figure 10. Rotation curve of the disks within our sample (red dots) of the ^{12}CO (left panels) and ^{13}CO (right panels) with the best-fit model using Equation (A13).
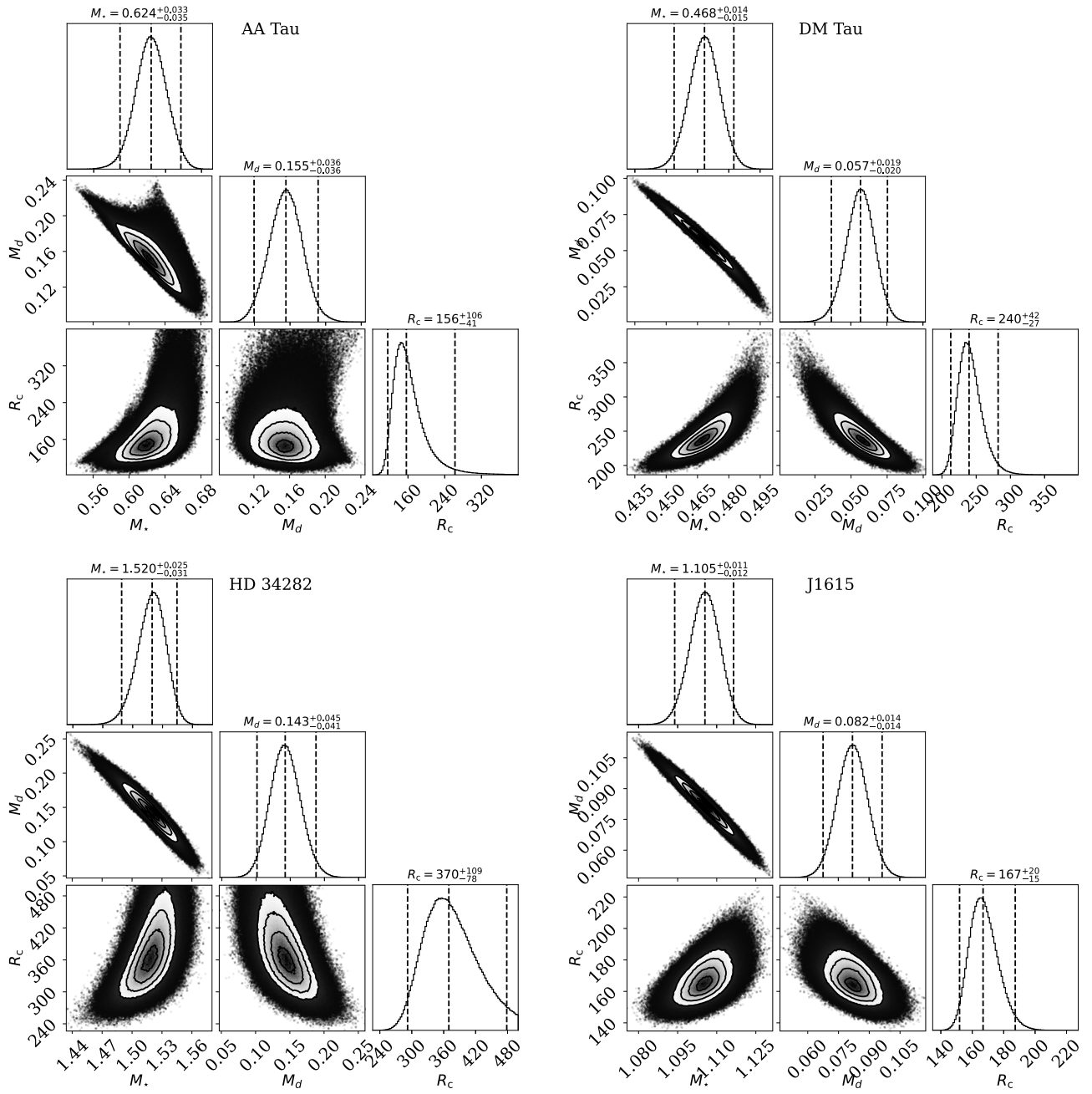
Figure 11. Corner plots for AA Tau, DM Tau, HD 34282, and J1615.
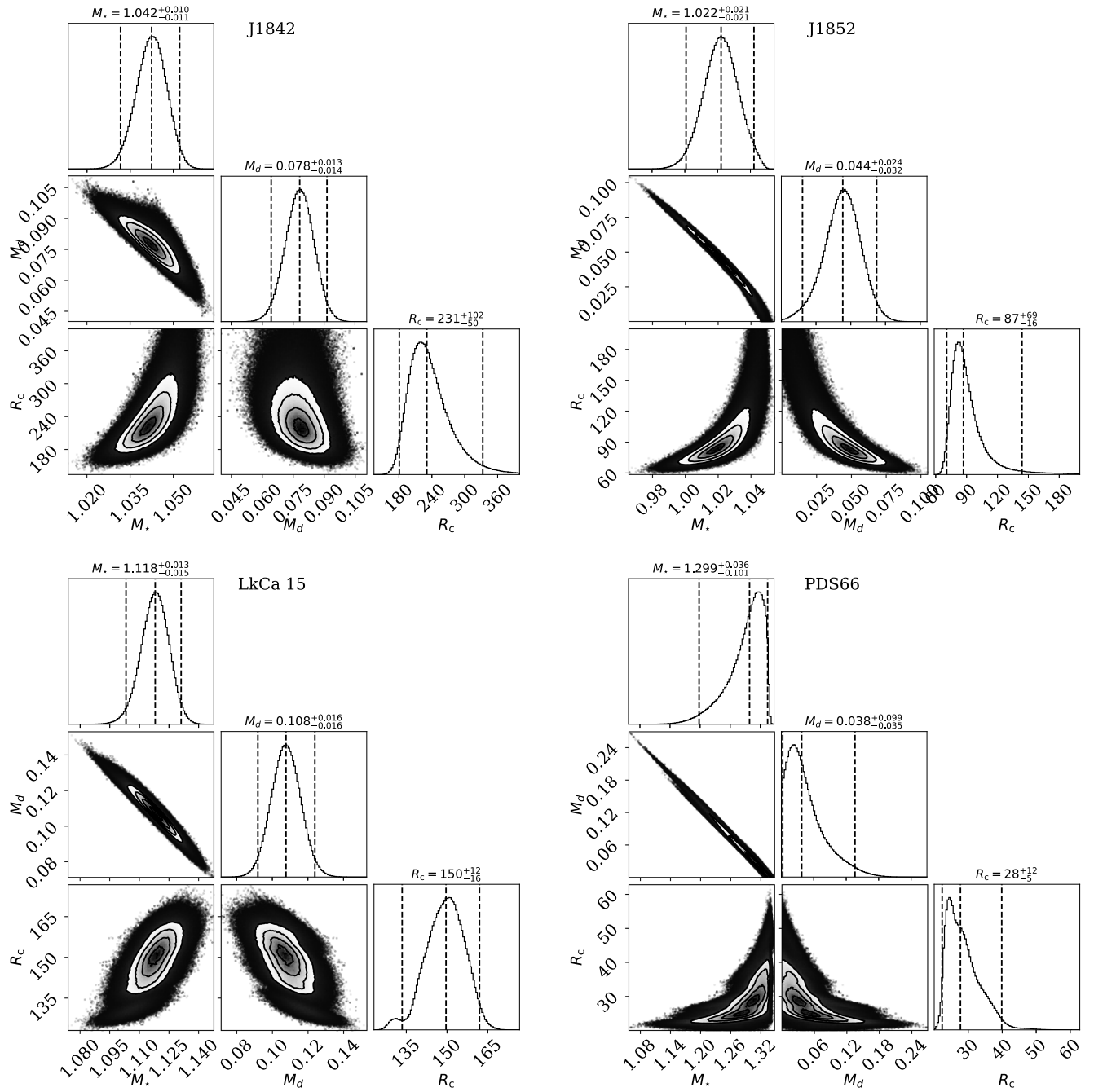
Figure 12. Corner plots for J1842, J1852, LkCa 15, and PDS 66.
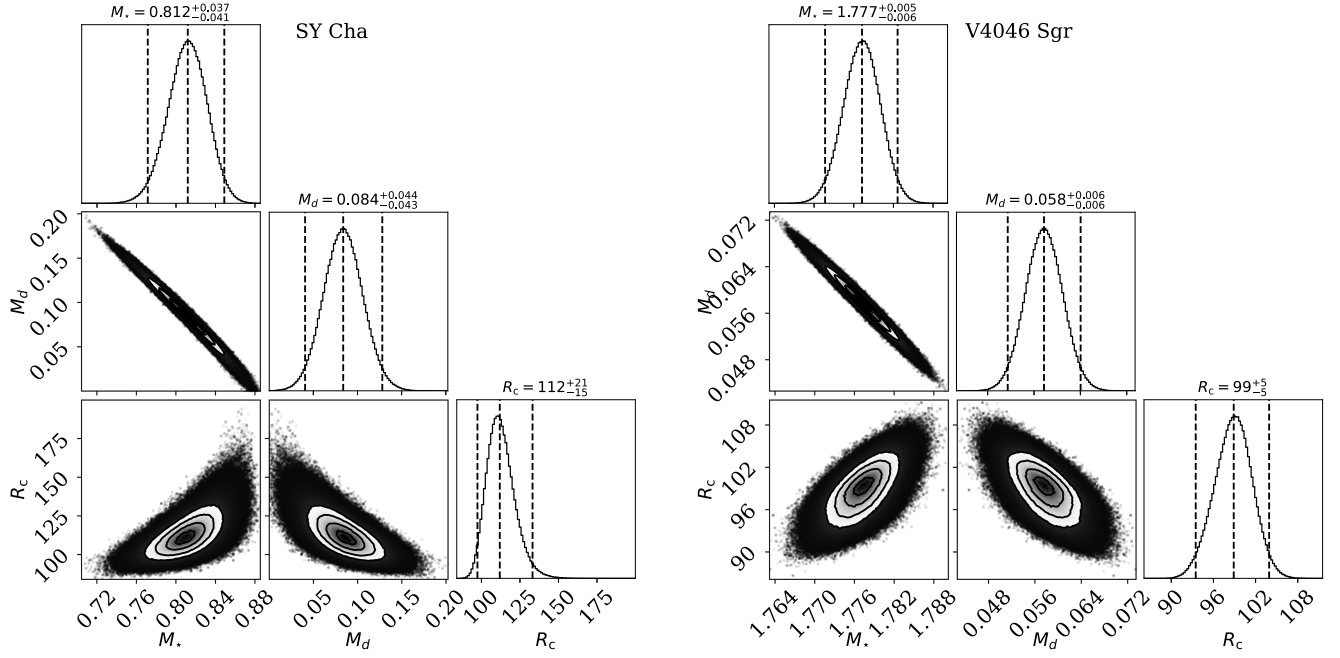
Figure 13. Corner plots for SY Cha and V4046 Sgr.

Appendix E
The Case of AA Tau

As pointed out in the main text of the Letter, we excluded the outer part of the ^{12}CO rotation curve from our fits. As a matter of fact, as pointed out by M. Galloway-Sprietsma et al. (2025), the signal coming from the outer disk of AA Tau is contaminated by the backside diffuse emission. As a result, the nonparametric emitting surface extracted by DISKSURF differs from the parametric one used by DISCMINER. Figure 14 shows the rotational velocity (upper panel) and the emitting height (lower panel) of the ^{12}CO emission of AA Tau. We note that the region contaminated by diffuse backside emission (>250 au) corresponds to an increase in the rotational velocity, which becomes highly super-Keplerian. This trend is possibly due to an extraction problem, and for this reason, we exclude this part of the disk from our analysis.
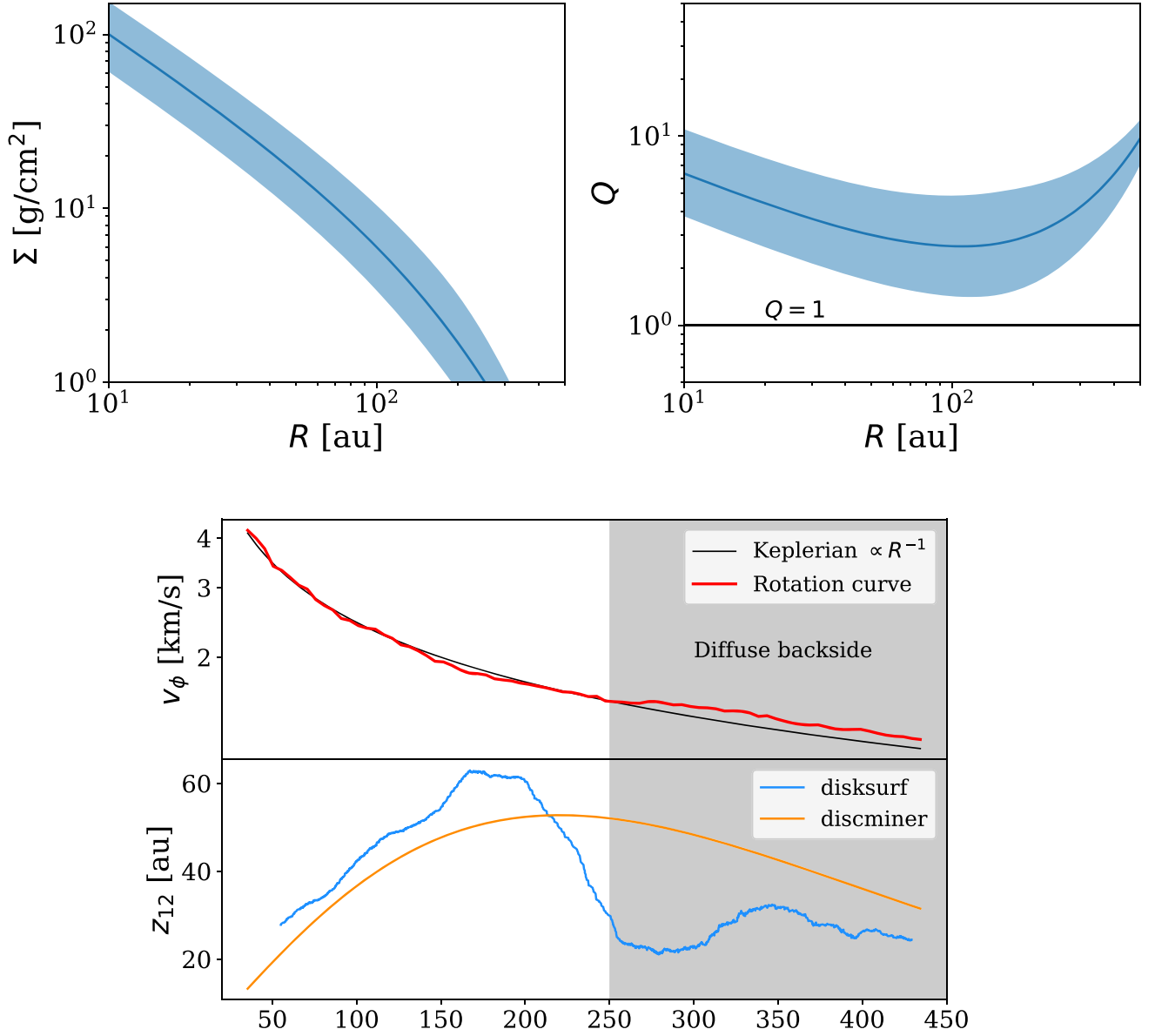
Figure 14. Top panel: surface density and Toomre Q profiles of AA Tau, where the error bar is computed by propagating the uncertainties on star and disk masses. Bottom panel: rotation curve of AA Tau compared to a Keplerian curve (top panel) and comparison between the nonparametric emitting layer of DISKSURF and the parametric of DISCMINER (bottom panel).

ORCID iDs

Cristiano Longarini ⓘ https://orcid.org/0000-0003-4663-0318
Giuseppe Lodato ⓘ https://orcid.org/0000-0002-2357-7692
Giovanni Rosotti ⓘ https://orcid.org/0000-0003-4853-5736
Sean Andrews ⓘ https://orcid.org/0000-0003-2253-2270
Andrew Winter ⓘ https://orcid.org/0000-0002-7501-9801
Jochen Stadler ⓘ https://orcid.org/0000-0002-0491-143X
Andrés Izquierdo ⓘ https://orcid.org/0000-0001-8446-3026
Maria Galloway-Sprietsma ⓘ https://orcid.org/0000-0002-5503-5476
Stefano Facchini ⓘ https://orcid.org/0000-0003-4689-2684
Pietro Curone ⓘ https://orcid.org/0000-0003-2045-2154
Myriam Benisty ⓘ https://orcid.org/0000-0002-7695-7605
Richard Teague ⓘ https://orcid.org/0000-0003-1534-5186
Jaehan Bae ⓘ https://orcid.org/0000-0001-7258-770X
Marcelo Barraza-Alfaro ⓘ https://orcid.org/0000-0001-6378-7873

Gianni Cataldi ⓘ https://orcid.org/0000-0002-2700-9676
Ian Czekala ⓘ https://orcid.org/0000-0002-1483-8811
Nicolás Cuello ⓘ https://orcid.org/0000-0003-3713-8073
Daniele Fasano ⓘ https://orcid.org/0000-0003-4679-4072
Mario Flock ⓘ https://orcid.org/0000-0002-9298-3029
Misato Fukagawa ⓘ https://orcid.org/0000-0003-1117-9213
Himanshi Garg ⓘ https://orcid.org/0000-0002-5910-4598
Cassandra Hall ⓘ https://orcid.org/0000-0002-8138-0425
Iain Hammond ⓘ https://orcid.org/0000-0003-1502-4315
Caitlyn Hardiman ⓘ https://orcid.org/0009-0003-7403-9207
Thomas Hilder ⓘ https://orcid.org/0000-0001-7641-5235
Jane Huang ⓘ https://orcid.org/0000-0001-6947-6072
John D. Ilee ⓘ https://orcid.org/0000-0003-1008-1142
Andrea Isella ⓘ https://orcid.org/0000-0001-8061-2207
Kazuhiro Kanagawa ⓘ https://orcid.org/0000-0001-7235-2417
Geoffroy Lesur ⓘ https://orcid.org/0000-0002-8896-9435

Ryan A. Loomis ⓘ https://orcid.org/0000-0002-8932-1219
Francois Ménard ⓘ https://orcid.org/0000-0002-1637-7393
Ryuta Orihara ⓘ https://orcid.org/0000-0003-4039-8933
Christophe Pinte ⓘ https://orcid.org/0000-0001-5907-5179
Daniel Price ⓘ https://orcid.org/0000-0002-4716-4235
Leonardo Testi ⓘ https://orcid.org/0000-0003-1859-3070
Gaylor Wafflard- Fernandez ⓘ https://orcid.org/0000-0002-3468-9577
Lisa Wölfer ⓘ https://orcid.org/0000-0002-7212-2416
Hsi-Wei Yen ⓘ https://orcid.org/0000-0003-1412-893X
Tomohiro C. Yoshida ⓘ https://orcid.org/0000-0001-8002-8473
Brianna Zawadzki ⓘ https://orcid.org/0000-0001-9319-1296

References

Abramowitz, M., & Stegun, I. A. 1970, Handbook of Mathematical Functions: with Formulas, Graphs, and Mathematical Tables (Washington, D.C.: U.S. Dept. of Commerce)

Andrews, S. M., Teague, R., Wirth, C. P., Huang, J., & Zhu, Z. 2024, ApJ, 970, 153

Andrews, S. M., Wilner, D. J., Hughes, A. M., Qi, C., & Dullemond, C. P. 2009, ApJ, 700, 1502

Andrews, S. M., Wilner, D. J., Hughes, A. M., Qi, C., & Dullemond, C. P. 2010, ApJ, 723, 1241

Ansdell, M., Williams, J. P., Trapman, L., et al. 2018, ApJ, 859, 21

Bertin, G., & Lodato, G. 1999, A&A, 350, 694

Birnstiel, T., & Andrews, S. M. 2014, ApJ, 780, 153

Braun, T. A. M., Yen, H.-W., Koch, P. M., et al. 2021, ApJ, 908, 46

Curone, P., Facchini, S., Andrews, S. M., et al. 2025, ApJL, 984, L9

Dartois, E., Dutrey, A., & Guilloteau, S. 2003, A&A, 399, 773

Donati, J. F., Gregory, S. G., Montmerle, T., et al. 2011, MNRAS, 417, 1747

Fairlamb, J. R., Oudmaijer, R. D., Mendigutìa, I., Ilee, J. D., & van den Ancker, M. E. 2015, MNRAS, 453, 976

Flaherty, K., Hughes, A. M., Simon, J. B., et al. 2020, ApJ, 895, 109

Flaherty, K., Hughes, A. M., Simon, J. B., et al. 2024, MNRAS, 532, 363

Flaherty, K. M., Hughes, A. M., Rosenfeld, K. A., et al. 2015, ApJ, 813, 99

Flaherty, K. M., Hughes, A. M., Rose, S. C., et al. 2017, ApJ, 843, 150

Foreman-Mackey, D., Hogg, D. W., Lang, D., & Goodman, J. 2013, PASP, 125, 306

Franceschi, R., Birnstiel, T., Henning, T., & Sharma, A. 2023, A&A, 671, A125

Galloway-Sprietsma, M., Bae, J., Izquierdo, A., et al. 2025, ApJL, 984, L10

Hartmann, L. 1998, Accretion Processes in Star Formation (Cambridge: Cambridge Univ. Press)

Ingleby, L., Calvet, N., Herczeg, G., et al. 2013, ApJ, 767, 112

Izquierdo, A., Stadler, J., Galloway-Sprietsma, M., et al. 2025, ApJL, 984, L8

Izquierdo, A. F., Testi, L., Facchini, S., Rosotti, G. P., & van Dishoeck, E. F. 2021, A&A, 650, A179

Izquierdo, A. F., Testi, L., Facchini, S., et al. 2023, A&A, 674, A113

Jin, S., Isella, A., Huang, P., et al. 2019, ApJ, 881, 108

Law, C. J., Teague, R., Loomis, R. A., et al. 2021, ApJS, 257, 4

Lin, C. C., & Shu, F. H. 1964, ApJ, 140, 646

Lodato, G., Rampinelli, L., Viscardi, E., et al. 2023, MNRAS, 518, 4481

Lynden-Bell, D., & Pringle, J. E. 1974, MNRAS, 168, 603

Manara, C. F., Ansdell, M., Rosotti, G. P., et al. 2023, in ASP Conf. Ser. 534, Protostars and Planets VII, ed. S. Inutsuka et al. (San Francisco, CA: ASP), 539

Manara, C. F., Testi, L., Natta, A., et al. 2014, A&A, 568, A18

Martire, P., Longarini, C., Lodato, G., et al. 2024, A&A, 686, A9

McClure, M. K., Bergin, E. A., Cleeves, L. I., et al. 2016, ApJ, 831, 167

Miotello, A., Kamp, I., Birnstiel, T., Cleeves, L. C., & Kataoka, A. 2023, in ASP Conf. Ser. 534, Protostars and Planets VII, ed. S. Inutsuka et al. (San Francisco, CA: ASP), 501

Miotello, A., van Dishoeck, E. F., Kama, M., & Bruderer, S. 2016, A&A, 594, A85

Öberg, K. I., Facchini, S., & Anderson, D. E. 2023, ARA&A, 61, 287

Öberg, K. I., Guzmán, V. V., Walsh, C., et al. 2021, ApJS, 257, 1

Paneque-Carreño, T., Izquierdo, A. F., Teague, R., et al. 2024, A&A, 684, A174

Pinte, C., Price, D. J., Ménard, F., et al. 2018, ApJL, 860, L13

Pinte, C., Teague, R., Flaherty, K., et al. 2023, in ASP Conf. Ser. 534, Protostars and Planets VII, ed. S. Inutsuka et al. (San Francisco, CA: ASP), 645

Rafikov, R. R. 2017, ApJ, 837, 163

Ribas, Á., Macìas, E., Weber, P., et al. 2023, A&A, 673, A77

Rosenfeld, K. A., Andrews, S. M., Hughes, A. M., Wilner, D. J., & Qi, C. 2013, ApJ, 774, 16

Rosotti, G., Longarini, C., Paneque-Carreño, T., et al. 2025, ApJL, 984, L20

Shakura, N. I., & Sunyaev, R. A. 1973, A&A, 24, 337

Simon, M., Dutrey, A., & Guilloteau, S. 2000, ApJ, 545, 1034

Simon, M., Guilloteau, S., Beck, T. L., et al. 2019, ApJ, 884, 42

Simon, M., Guilloteau, S., Di Folco, E., et al. 2017, ApJ, 844, 158

Stadler, J., Benisty, M., Winter, A., et al. 2025, ApJL, 984, L11

Stapper, L. M., Hogerheijde, M. R., van Dishoeck, E. F., et al. 2024, A&A, 682, A149

Stempels, H. C., & Gahm, G. F. 2004, A&A, 421, 1159

Sturm, J. A., Booth, A. S., McClure, M. K., Leemker, M., & van Dishoeck, E. F. 2023, A&A, 670, A12

Tabone, B., Rosotti, G. P., Cridland, A. J., Armitage, P. J., & Lodato, G. 2022, MNRAS, 512, 2290

Teague, R., Benisty, M., Facchini, S., et al. 2025, ApJL, 984, L6

Toci, C., Lodato, G., Livio, F. G., Rosotti, G., & Trapman, L. 2023, MNRAS, 518, L69

Toci, C., Rosotti, G., Lodato, G., Testi, L., & Trapman, L. 2021, MNRAS, 507, 818

Toomre, A. 1964, ApJ, 139, 1217

Trapman, L., Longarini, C., Rosotti, G., et al. 2025, ApJL, 984, L18

Trapman, L., Rosotti, G., Zhang, K., & Tabone, B. 2023, ApJ, 954, 41

Trapman, L., Zhang, K., van't Hoff, M. L. R., Hogerheijde, M. R., & Bergin, E. A. 2022, ApJL, 926, L2

van der Marel, N., Birnstiel, T., Garufi, A., et al. 2021, AJ, 161, 33

Veronesi, B., Longarini, C., Lodato, G., et al. 2024, A&A, 688, A136

Veronesi, B., Paneque-Carreño, T., Lodato, G., et al. 2021, ApJL, 914, L27

Williams, J. P., & Best, W. M. J. 2014, ApJ, 788, 59